

# Angle-resolved photoemission study of the evolution of band structure and charge density wave properties in $R\text{Te}_3$ ( $R=\text{Y, La, Ce, Sm, Gd, Tb, and Dy}$ )

V. Brouet,<sup>1,2,3</sup> W. L. Yang,<sup>2,3</sup> X. J. Zhou,<sup>2,3</sup> Z. Hussain,<sup>2</sup> R. G. Moore,<sup>3,4</sup> R. He,<sup>3,4</sup> D. H. Lu,<sup>3</sup> Z. X. Shen,<sup>2,3,4</sup> J. Laverock,<sup>5</sup> S. B. Dugdale,<sup>5</sup> N. Ru,<sup>4</sup> and I. R. Fisher<sup>4</sup>

<sup>1</sup>Laboratoire Physique des Solides, UMR8502, CNRS, Université Paris-Sud XI, Bâtiment 510, 91405 Orsay, France

<sup>2</sup>Advanced Light Source, Lawrence Berkeley National Laboratory, Berkeley, California 94720, USA

<sup>3</sup>Stanford Synchrotron Radiation Laboratory, Stanford University, Stanford, California 94305, USA

<sup>4</sup>Geballe Laboratory for Advanced Materials and Department of Applied Physics, Stanford University, Stanford, California 94305-4045, USA

<sup>5</sup>H. H. Wills Physics Laboratory, University of Bristol, Tyndall Avenue, Bristol BS8 1TL, United Kingdom

(Received 16 January 2008; published 4 June 2008)

We present a detailed angle-resolved photoemission spectroscopy (ARPES) investigation of the  $R\text{Te}_3$  family, which sets this system as an ideal “textbook” example for the formation of a nesting driven charge density wave (CDW). This family indeed exhibits the full range of phenomena that can be associated to CDW instabilities, from the opening of large gaps on the best nested parts of Fermi surface (up to 0.4 eV), to the existence of residual metallic pockets. ARPES is the best suited technique to characterize these features, thanks to its unique ability to resolve the electronic structure in  $k$  space. An additional advantage of  $R\text{Te}_3$  is that the band structure can be very accurately described by a simple two dimensional tight-binding (TB) model, which allows one to understand and easily reproduce many characteristics of the CDW. In this paper, we first establish the main features of the electronic structure by comparing our ARPES measurements with the linear muffin-tin orbital band calculations. We use this to define the validity and limits of the TB model. We then present a complete description of the CDW properties and of their strong evolution as a function of  $R$ . Using simple models, we are able to reproduce perfectly the evolution of gaps in  $k$  space, the evolution of the CDW wave vector with  $R$ , and the shape of the residual metallic pockets. Finally, we give an estimation of the CDW interaction parameters and find that the change in the electronic density of states  $n(E_F)$ , due to lattice expansion when different  $R$  ions are inserted, has the correct order of magnitude to explain the evolution of the CDW properties.

DOI: [10.1103/PhysRevB.77.235104](https://doi.org/10.1103/PhysRevB.77.235104)

PACS number(s): 71.45.Lr, 71.18.+y, 79.60.-i

## I. INTRODUCTION

Charge density waves (CDWs) are typical instabilities of the Fermi surface (FS) in the presence of electron-phonon coupling.<sup>1</sup> They occur when many electrons can be excited with the same  $q$  vector of one particular phonon mode at a moderate energy cost, i.e., by keeping these electrons near the Fermi level. The ideal case is when *all* electrons can be excited this way, which implies that all parts of FS can be connected by  $q$  to some other parts. This property of the FS is called the perfect nesting. For an ideal one dimensional (1D) system, the FS consists of two points, at  $-k_F$  and  $+k_F$ , so that it exhibits by definition the perfect nesting at  $q=2k_F$ . Hence, all 1D systems are subject to CDW transitions, often called the Peierls transitions in this case. In real systems, the good nesting properties are usually reduced to some particular regions of the FS but are nevertheless often sufficient to trigger CDWs [or spin density waves (SDWs), their spin analog] in many quasi-1D, two dimensional (2D) or even three dimensional (3D) systems (a famous example is the SDW of  $\text{Cr}^2$ ). In this case, the CDW/SDW gap is expected to open only on the best nested FS parts and the system may remain metallic in its broken symmetry ground state.

Although these ideas were introduced in the 1950s and CDWs were heavily studied experimentally since the mid-1970s,<sup>3</sup> they remain a subject of interest for today’s research because of the continued interest in the complicated

physics of low dimensional systems. In these systems, CDWs or SDWs are often instabilities competing with more exotic ground states, and they are therefore important to fully characterize. For example, Yao *et al.*<sup>4</sup> used  $R\text{Te}_3$  to study the competition between checkerboard and striped charge orders, which may be of relevance for comparison with cuprates or nickelates.

Also, the technical progress of angle-resolved photoemission spectroscopy (ARPES) in the past two decades has made it possible, in principle, to illustrate very elegantly the impact of the CDW formation on the electronic structure, in a much more direct way than with any other experimental methods. As ARPES produces images of the FS, one can directly examine its nesting properties and compare them with the strength of the CDW gap measured on the different FS parts. Despite this, there are not many examples of CDW systems, where ARPES could be used to illustrate all these points. This is mainly because finding a truly low dimensional system that remains relatively simple is a rather difficult task. As we have seen, quasi-1D systems are the most likely hosts for CDW. However, they also exhibit by nature serious deviations from the Fermi-liquid theory that complicates ARPES analysis. In particular, Fermi edges are usually not well defined, making the definition of gaps more difficult, as in organic conductors,<sup>5</sup>  $(\text{TaSe}_4)_2\text{I}^6$  or  $\text{K}_{0.3}\text{MoO}_3$ .<sup>6,7</sup> Also, for a truly 1D system, the gap would open homogeneously on the FS, which reduces the interest of a  $k$ -resolved

probe such as ARPES. In the quasi-1D system NbSe<sub>3</sub>, imperfect nesting gives rise to coexistence between gapped and metallic regions, which could be observed in ARPES,<sup>8</sup> despite a rather complicated band structure. Hence, quasi-2D systems appear as a more simple choice for photoemission studies. Transition metal chalcogenides ( $1T$ - $MX_2$  or  $2H$ - $MX_2$  with  $M$ =Ti, Nb, Ta and  $X$ =S, Se, Te) exhibit a variety of quasi-2D CDW behaviors that have been extensively studied with ARPES.<sup>5,9</sup> Despite this, no simple relation between nesting properties and the reported gaps (usually 10–20 meV) could be firmly established<sup>9,10</sup> and the mechanism of the CDW itself is still debated.<sup>11</sup> Let us emphasize that despite the presence of chalcogenides, these systems have little in common with  $R\text{Te}_3$ . Triangular planes of transition metal ions dominate their electronic properties, while these are square planes of Te in  $R\text{Te}_3$ . The  $R_3\text{Ir}_4\text{Si}_{10}$  ( $R$ =Dy-Lu) system offers an interesting situation,<sup>12</sup> where the CDW transition can be tuned from 80 to 160 K as a function of  $R$ , but their 3D structure has limited so far the possibilities of ARPES studies. To conclude this short overview of ARPES in CDW systems, let us mention the case of the surface CDW in In/Cu(001),<sup>13</sup> which exhibits interesting similarities with  $R\text{Te}_3$ , although it is not a bulk phase transition.

$R\text{Te}_3$  are quasi-2D metals, where a much clearer situation is encountered. We will argue that they do allow the illustration of the main CDW concepts fairly well and further raise interesting questions on the limits of different CDW models. After the seminal work initiated by DiMasi *et al.*,<sup>14–16</sup> there has been a growing wealth of information about these materials gathered through detailed structural,<sup>17,18</sup> scanning tunneling microscopy (STM),<sup>17,19</sup> ARPES,<sup>20,21</sup> transport,<sup>22</sup> and optical studies.<sup>23,24</sup> It was first believed that these compounds always remain in the CDW state, up to their melting point, making the language of phase transition questionable. We have recently revealed a transition to the normal state at 244 K in TmTe<sub>3</sub> up to 416 K in SmTe<sub>3</sub> and presumably even higher temperature for lighter  $R$ .<sup>18</sup> This definitely qualifies this family as CDW materials and opens perspectives for a full characterization of the CDW state, including the fluctuations above the transition. In this paper, we will restrict our study to the characterization of the ground state of the light rare earths from LaTe<sub>3</sub> to DyTe<sub>3</sub>. For the heavy rare earth (DyTe<sub>3</sub> and above), two successive phase transitions occur,<sup>18</sup> which we do not consider here. The possibility of tuning the CDW properties (the transition temperature, the size of the gap, and the wave vector  $q_{\text{CDW}}$ ) with  $R$  is a rather unique property of this family (see also Ref. 12), which is very useful to discuss the origin of the CDW. A similar variation of the CDW properties can be induced by applied pressure,<sup>24</sup> making it likely that the changes are due to lattice contraction.

The CDW in  $R\text{Te}_3$  is characterized by large displacements (about 0.2 Å) (Ref. 17) and large gaps in the electronic structure (up to 0.4 eV).<sup>20,21,23</sup> This large gap is an advantage for ARPES studies because it makes it easy to measure its location and changes in  $k$  space accurately. On the other hand, it raises questions about the nature of the CDW and especially whether the traditional weak coupling treatment of the nesting driven CDW would still hold. Indeed, the gap is presumably several times larger than the phonon frequencies

involved. In such a situation, a strong coupling model of the CDW could appear more appropriate, where the structural distortion is really the driving force for the transition. The local tendency of Te atoms to form stable chemical bonds would be its starting point. Indeed, a usual Te-Te bond is 2.8 Å, whereas the average distance between Te in the planes hosting the CDW is about 3.1 Å. Whangbo and Canadell<sup>25</sup> discussed, in the case of  $1T$ - or  $2H$ - $MX_2$ , the similarities and differences between the approach of FS nesting or chemical bonding. More recently, Johannes and Mazin<sup>26</sup> emphasized the crucial role of the lattice distortion in triggering the transition for various CDW systems, including CeTe<sub>3</sub>. The distinction between weak and strong CDWs was investigated by Nakagawa *et al.*<sup>13</sup> in their study of In/Cu(001). They concluded that the CDW in this system was of “dual nature.” In this paper, we will show, with unprecedented details for any CDW system, that the predictions of the FS nesting scenario explain extremely well the openings of gaps observed by ARPES in  $R\text{Te}_3$ . Furthermore, the main variations of the CDW properties with  $R$  can be well explained by an additional stabilization of the CDW due to the enhancement of  $n(E_F)$  through lattice contraction. This gives substantial ground that the electronic energy is, at least, an essential ingredient for the formation of the CDW in  $R\text{Te}_3$ .

Large single crystals of  $R\text{Te}_3$  were grown by slow cooling of a binary melt.<sup>22</sup> The crystals easily cleave between two Te planes,<sup>19</sup> providing a good surface quality for ARPES. ARPES measurements were mostly carried out at the beamline (BL) 10.0.1 of the Advanced Light Source (ALS), with a Scienta-2002 analyzer, an energy resolution better than 20 meV and an angular resolution of 0.3°. Other data were acquired at BL 12 of the ALS (Figs. 7 and 12) and BL 5–4 of the Stanford Synchrotron Radiation Laboratory (Fig. 11). All measurements were performed at low temperatures,  $T \approx 20$  K.

## II. TIGHT-BINDING MODEL OF THE ELECTRONIC STRUCTURE

In  $R\text{Te}_3$ , Te planes are stacked with  $R/\text{Te}$  slabs,<sup>27</sup> as sketched in Fig. 1(a). Note that we follow the usual convention where the  $b$  axis is *perpendicular* to the Te planes ( $b \approx 26$  Å). The planar unit cell [(a) and (c)] is defined by the  $R$  atoms of the slab [light gray (orange) square in Figs. 1(a) and 1(b)]. There is a small orthorhombic distortion of this square, which shrinks from  $a=4.405$  Å and  $c=4.42$  Å in LaTe<sub>3</sub> to  $a=4.302$  Å and  $c=4.304$  Å in DyTe<sub>3</sub>.<sup>18</sup> The Te atoms in the planes form a nearly square net but with a square unit [dark gray (green) square] rotated by 45° with respect to the unit cell and with only half the area. Hence, two different Brillouin zones (BZ) will be convenient to use throughout this paper: a 2D BZ built on the Te square from the plane and the 3D BZ built on the lattice unit cell [see Fig. 1(c)]. We define  $a^*=2\pi/a$  and  $c^*=2\pi/c$  as unit wave vectors of the 3D BZ.

The band structure was calculated using the linear muffin-tin orbital (LMTO) method for a fictitious LuTe<sub>3</sub> composition and  $a=c=4.34$  Å.<sup>28</sup> Lu was chosen to avoid the complications associated with the description of  $f$  electrons in the

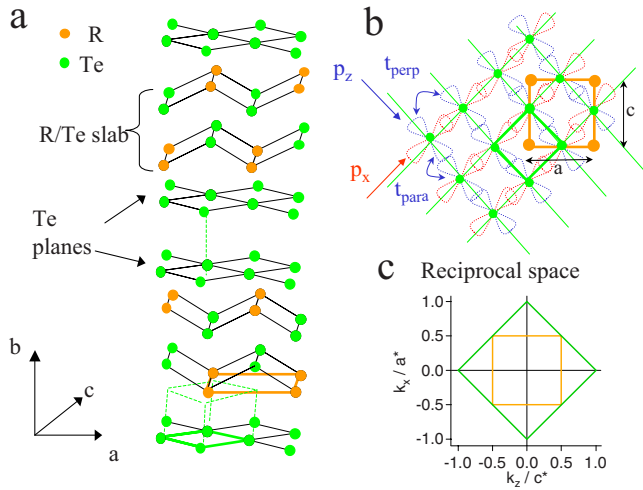


FIG. 1. (Color online) (a) Sketch of the  $R\text{Te}_3$  structure. (b) Sketch of the Te plane [dark gray (green) points] with in-plane  $p_x$  and  $p_z$  orbitals. [(a) and (c)] The 3D unit cell is shown as light gray (orange) square. (c). Sketch of the reciprocal space with the 3D BZ [light gray (orange)] and the 2D BZ [dark gray (green)], which would correspond to one isolated Te plane.

local-density approximation. The calculated band structure is shown in Fig. 2(a) along  $c^*$  at a fixed  $k_x=0.3a^*$  and  $k_y=0$ . There are 18 different bands found between 2 and  $-6$  eV, corresponding to the Te  $5p$  orbitals of the six Te per unit cell (two in the slab and four in the planes). However, only four bands cross the Fermi level, corresponding to the Te in-plane  $p_x$  and  $p_z$  orbitals. They are well isolated from other bands over a 1 eV window below  $E_F$ .

The dispersion of these bands can be very well reproduced by a tight-binding (TB) model of the Te plane. We

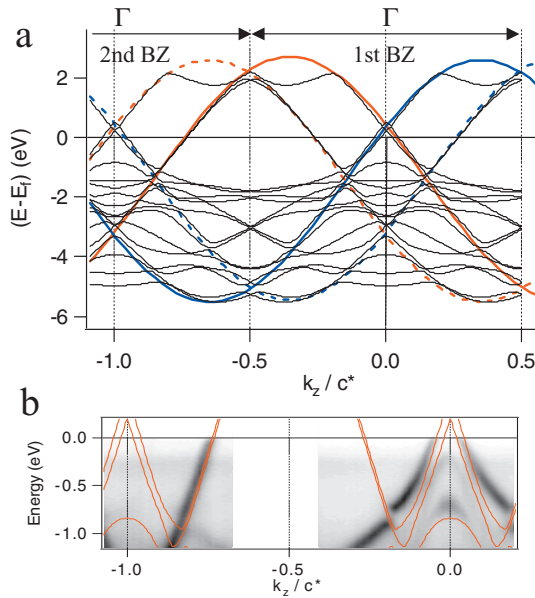


FIG. 2. (Color) (a) Band structure along  $c^*$  for  $k_x=0.3a^*$  and  $k_y=0$  calculated with LMTO method. The red and blue lines are TB fits for  $p_x$  and  $p_z$ . The dotted lines are folded bands. (b) Zoom in of the electronic structure near  $E_F$  measured with ARPES in  $\text{CeTe}_3$  at 55 eV along the same direction. The red lines are the LMTO calculated bands.

consider only the two perpendicular chains of  $p_x$  and  $p_z$  orbitals, represented on Fig. 1(b) in red and blue, with a coupling  $t_{\text{para}}$  along the chain and  $t_{\text{perp}}$  perpendicular to the chains. We assume a square net and totally neglect the coupling between  $p_x$  and  $p_z$ . Using the axes of the 3D BZ, this yields the following dispersions:

$$E_{p_x}(k_x, k_z) = -2t_{\text{para}} * \cos[(k_x + k_z) * a/2] - 2t_{\text{perp}} * \cos[(k_x - k_z) * a/2] - E_F,$$

$$E_{p_z}(k_x, k_z) = -2t_{\text{para}} * \cos[(k_x - k_z) * a/2] - 2t_{\text{perp}} * \cos[(k_x + k_z) * a/2] - E_F.$$

This model is plotted on top of the calculated band structure in Fig. 2(a), as red and blue lines for  $p_x$  and  $p_z$ , respectively. As the TB bands are constructed for one Te plane, they have the periodicity of the 2D BZ and they have to be folded back with respect to the 3D BZ boundaries to acquire the 3D lattice symmetry. These additional folded bands are shown as dotted lines in Fig. 2(a). The Fermi level  $E_F = -2t_{\text{para}} \sin(\pi/8)$  was fixed so that  $p_x$  and  $p_z$  each contains 1.25 electrons. We assume here that all  $R$  are trivalent<sup>16,22</sup> and donate two electrons to each Te in the slab and 0.5 electrons to each Te of the two planes. We further assume that the out-of-plane Te orbital  $p_y$  is completely filled, leaving 2.5 electrons for  $p_x$  and  $p_z$ . The TB parameters were adjusted to reproduce best the calculated band structure, which is reached for  $t_{\text{para}} = -1.9$  eV and  $t_{\text{perp}} = 0.35$  eV. It is worth noting that although  $|t_{\text{perp}}| \ll |t_{\text{para}}|$ , it is much larger than the temperature ( $t_{\text{perp}} \approx 3000$  K), so that one would not be in a 1D limit, even for an isolated set of chains. As there are two Te planes per unit cell, the bands in the calculation are doubled and there is a clear “bilayer splitting” between them. In this calculation, spin-orbit couplings were neglected.

Figure 2(b) shows the corresponding electronic structure measured with ARPES. The calculation indicates very well the positions and slopes of the bands near the Fermi level, except that the intensity of the folded bands [dotted lines in Fig. 2(a)] is so weak that they are hardly distinguishable. As explained in Ref. 21, the intensity of the folded bands is very generally proportional to the strength of the coupling responsible for the folding. The weak intensity of the folded bands reflects here the small 3D couplings and, consequently, the nearly 2D character of these compounds. For the deeper Te bands, we observe some deviations between the calculated and measured bands; more details will be given in Sec. II C 2.

The excellent description of the electronic structure near  $E_F$  with only in-plane Te orbitals suggests a negligible coupling with the  $R/\text{Te}$  slab. The transport anisotropy is indeed very large, at least a factor 100.<sup>16,22</sup> In this case, one expects that the main consequence of changing  $R$  will be a change in bandwidth due to the expansion or contraction of the Te square lattice. Figure 3 displays the ARPES intensity of the Te bands integrated around the  $\Gamma$  point for different rare earths. Their structure is quite similar, confirming the small influence of rare-earth orbitals. The total bandwidth can be estimated by the peak position of the last band. It increases

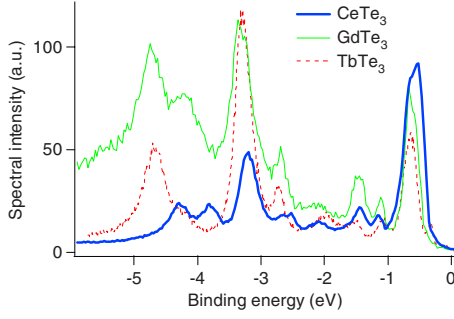


FIG. 3. (Color online) Te valence bands integrated around the  $\Gamma$  point, measured for different rare earths, at a photon energy of 55 eV.

from about 4.25 eV for Ce ( $c=4.385 \text{ \AA}$ ) to 4.70 eV in Gd ( $c=4.33 \text{ \AA}$ ) and Tb ( $c=4.314 \text{ \AA}$ ). This is in qualitative agreement with the larger overlaps between Te orbitals expected for smaller lattice parameters.

In our calculation, the bandwidth at  $\Gamma$  increases when contracting the lattice from 4.75 eV (La,  $c=4.42 \text{ \AA}$ ) to 5.15 eV (Dy,  $c=4.03 \text{ \AA}$ ), i.e., by 8%. While these absolute values are a little larger than the experimental ones, the order of magnitude of the expansion is in good agreement. This corresponds in the calculation to a decrease in the density of states (DOS) at the Fermi level from  $n(E_F)=1.6$  (La) to 1.5 states/eV/cell (Dy). With the TB model, for  $t_{\text{para}}=-1.9 \text{ eV}$  and  $t_{\text{perp}}=0.35 \text{ eV}$  estimated before for  $a=c=4.34 \text{ \AA}$ , we calculate  $n(E_F)=1.48$  states/eV/cell slightly smaller. This is the same trend as for the bandwidth and suggests that a slightly smaller value of  $t_{\text{para}}$  might be more appropriate to describe  $R\text{Te}_3$ . We observe that  $n(E_F)$  solely depends on  $t_{\text{para}}$  for realistic values of  $t_{\text{perp}}$ . To reproduce the calculated  $n(E_F)$  values, one has to use  $t_{\text{para}}=-1.7$  (La) to  $-1.85 \text{ eV}$  (Dy). This is a variation of 8%, in good agreement with that of the bandwidth, both calculated and experimentally observed. Therefore, we will use this parameter range in the rest of the paper to model the changes in the electronic structure from La to Dy.

### A. Fermi surface

The FS expected in the TB model is very simple. It is made out of two perpendicular sets of nearly parallel lines,

corresponding to the two chains. They are shown in Fig. 4(a) in red and blue for  $p_x$  and  $p_z$ , respectively. With no perpendicular coupling ( $t_{\text{perp}}=0$ ), the problem would be reduced to that of two perfectly 1D chains, perpendicular to each other, and the FS would consist of two sets of exactly straight lines, exhibiting perfect nesting.<sup>15</sup> The coupling between the chains introduces a deviation from one dimensionality and a curvature of the FS proportional to  $|t_{\text{perp}}/t_{\text{para}}|$ . We will show in Sec. III (e.g., Fig. 17) that it is precisely this curvature that makes the nesting imperfect. The arrow indicates the best nesting wave vector  $q_N=0.68c^*$ . There are other wave vectors giving better (actually perfect) nesting for  $p_x$  or  $p_z$ , but this one reaches a better compromise by nesting equivalently  $p_x$  and  $p_z$ . The competition between these different wave vectors has been studied by Yao *et al.*<sup>4</sup>

The TB FS in Fig. 4(a) is shown for the two sets of parameters corresponding to Dy and La. The two contours are, however, so close that they cannot be distinguished. This is normal, as the FS area should be proportional to the number of holes in the band, which is kept constant in our model. A change in the FS contour would violate the Luttinger theorem.<sup>29</sup> When the bandwidth changes, the Fermi level readjusts to keep this contour constant, and the FS is therefore strictly independent of  $t_{\text{para}}$ . This means that, within this model, the *nesting properties* remain exactly the same throughout the series.

The experimental FS of  $R\text{Te}_3$  was first measured by Gweon *et al.*<sup>20</sup> in  $\text{SmTe}_3$ . In Fig. 5, we present the FS for different  $R=Y, \text{Ce}, \text{and Sm}$ , compared to the predictions of the TB model. The FS is obtained by integration of the spectral weight in a 10 meV window around  $E_F$ . The spectral weight is strongly suppressed in a large region around  $k_x=0$  (note that the axes are rotated for  $\text{YTe}_3$ ). We will show in Sec. III that this is due to the opening of a large CDW gap in these regions. Although the directions of  $k_x$  and  $k_z$  appear at first quite similar in structure, x-ray measurements have shown that the gap is always open along the  $c$  axis.<sup>18</sup> Accordingly, we only observe the gap opening along  $k_z$ . These regions are the best nested ones (see Fig. 17); in those with poorer nesting, the gap does not open at the Fermi level and we observe again intensity at  $E_F$ . Interestingly, the ungapped regions appear larger in  $\text{YTe}_3$  and  $\text{SmTe}_3$  than  $\text{CeTe}_3$  (this is particularly clear for the ungapped fraction of the square).

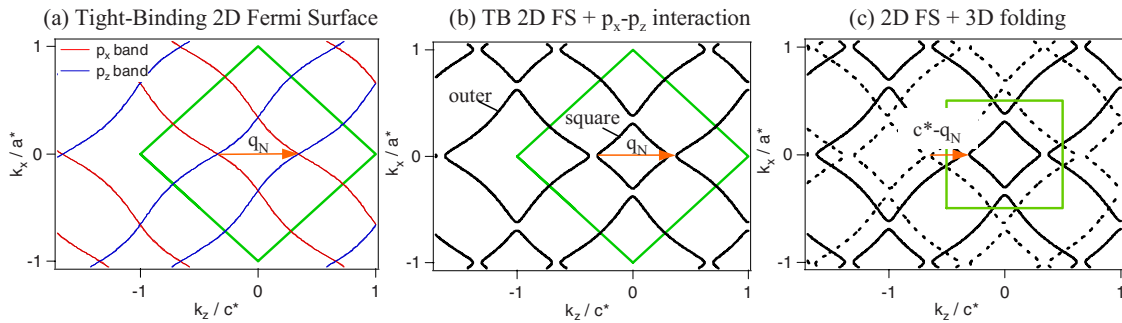


FIG. 4. (Color online) (a) Tight binding FS for ( $t_{\text{para}}=-1.7 \text{ eV}$ ,  $t_{\text{perp}}=0.35 \text{ eV}$ ) and ( $t_{\text{para}}=-1.85 \text{ eV}$ ,  $t_{\text{perp}}=0.35 \text{ eV}$ ). The two contours overlap almost perfectly (see text). The square delimits the BZ corresponding to one Te plane. The arrow represents the best nesting wave vector  $q_N$ . (b) Same as (a) after interaction between  $p_x$  and  $p_z$  that separates the square part of FS from the outer part. (c) Same as (b) plus, as dotted lines, the FS contours folded with respect to the 3D BZ limits (small square). The arrow represents the equivalent nesting direction but defined in the 3D BZ ( $c^*-q_N$ ).

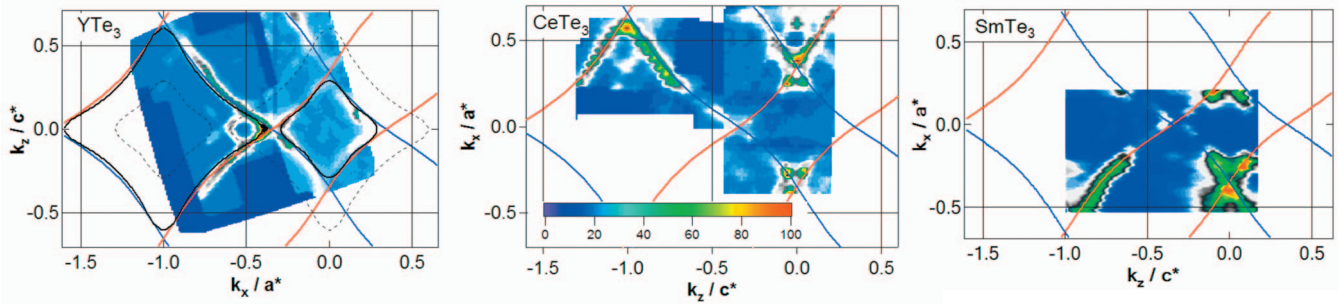


FIG. 5. (Color) Fermi surface for  $\text{YTe}_3$ ,  $\text{CeTe}_3$ , and  $\text{SmTe}_3$ , obtained by integration of spectral weight in a 10 meV window around  $E_F$ . No symmetry operation was applied to the data. Photon energy was 35 eV for  $\text{YTe}_3$  and 55 eV for  $\text{CeTe}_3$  and  $\text{SmTe}_3$ ; polarization was almost perpendicular to the sample surface. The red and blue lines correspond to the Fermi surface calculated with the TB model described in the text. The black contours on  $\text{YTe}_3$  map are guides for the eyes for the shape of square and outer pieces of FS. The suppression of spectral weight around  $k_x=0$  is due to the opening of the CDW gap (note that  $\text{YTe}_3$  map is rotated by  $90^\circ$ ).

We will analyze this behavior quantitatively in Sec. III and show that it can be understood from the larger gap of  $\text{CeTe}_3$ .

Clearly, the distribution of the spectral intensity is equally well described by the TB model in the three cases and this was true for all the rare earths we have measured. As discussed before, this does not give information on  $t_{\text{para}}$  but rather proves that there are no significant changes in the band filling. This is not a trivial result as is, for example, not the case in  $R\text{Te}_2$ .<sup>30</sup> On the other hand, the well-defined curvature of the FS allows us to estimate  $t_{\text{perp}}=0.35 \pm 0.08$  eV. This is a totally independent estimation from Sec. I, but turns out to be in very good agreement.

The major deviation between the experimental FS and the TB fit takes place at the crossing between  $p_x$  and  $p_z$ . This is because there is no coupling between these bands considered in our TB model. Figure 5 shows that, in reality, they do interact and this rounds the FS contours near the crossings. This effect is simulated in Fig. 4(b); It creates two different sheets of FS: a small holelike piece around  $\Gamma$ , called hereafter “square,” and a larger electronlike piece mainly in the second BZs, called hereafter “outer.” Note that the nesting quality and the wave vector do not change when this interaction is added because the effect is symmetric on the square and outer FSs that are nested into one another.

In the 3D BZ, the folding of the FS gives rise to the dotted black contours of Fig. 4(c). Experimentally, Fig. 5 shows that their intensity is always very weak, except near the zone boundaries.<sup>21</sup> The nesting properties are the same, except they would be described by  $(c^*-q_N)$  in the 3D BZ.

### B. Dispersion

In Fig. 2, one can check that not only the position of the FS crossings but also the slopes of the dispersions are in very good agreement with the TB model. This value directly depends on  $t_{\text{para}}$ , so that its evolution as a function of rare earth may give additional insights into the evolution of the electronic structure.

Metallic properties are best measured on the outer part of FS, where the line shape is more simple (see parts C and D). Near  $E_F$ , the dispersion is nearly linear and we extract its slope by a linear fit over a 0.2 eV window. We observe that

the changes in the slope of the dispersion are small along the outer FS and also as a function of  $R$ . In fact, the slope essentially depends on the direction in which the dispersion is measured, i.e., the angle  $\alpha$  of the detector slits of the analyzer with respect to  $k_z$  axis.

The TB model again offers a useful guide to understand this evolution. As the bands are essentially one dimensional, the slope of the dispersion is nearly constant when measured along the chain direction (i.e.,  $\alpha = \pm 45^\circ$ ). We define this value as the reference Fermi velocity, which is  $V_F = \sqrt{2}at_{\text{para}} \sin(k_F a)$ . On the other hand, the slope of the dispersion rapidly falls to zero if measured perpendicularly to the chain. This dependence is illustrated on Fig. 6(a) for the two values of  $k_x$  between which the dispersion can be measured reliably on the outer FS. It is nearly a cosine function of  $\alpha$  and only the small  $t_{\text{perp}}$  gives it some  $k_x$  dependence. Many different values measured for different samples and/or branches of the FS are reported as the color points. The variation with  $k_x$  is indeed within the error bar of the measurement and the general trend is the dependence with  $\alpha$ . In Fig. 6(b), we plot  $V_F$  as a function of the lattice parameter  $c$ , after correcting for the  $\alpha$  dependence. We obtain an average value for all samples,  $V_F = 10 \pm 1$  eV  $\text{\AA}$ . Within the TB

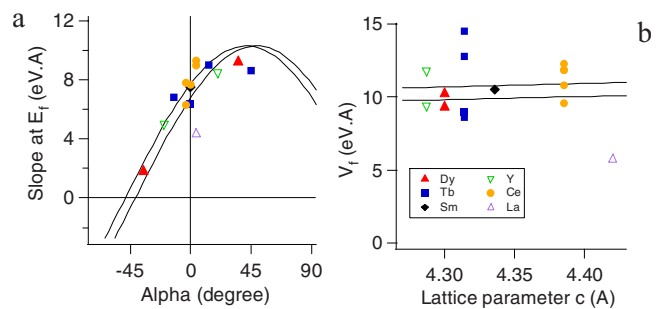


FIG. 6. (Color online) (a) Color points: measured values of the slope of dispersion for different  $R\text{Te}_3$  compounds and different branches of FS, as a function of the angle  $\alpha$  of the measurement. Black lines: variation of the slope of the dispersion near  $E_F$ , calculated in the TB model, for  $k_x=0.6a^*$  and  $0.7a^*$ ,  $t_{\text{para}}=-1.7$  eV and  $t_{\text{perp}}=0.35$  eV. (b)  $V_F$  values corrected for the  $\alpha$  dependence as a function of lattice parameter. The black lines are theoretical variations of  $V_F$  for  $t_{\text{para}}=-1.7$  and  $-1.85$  eV.

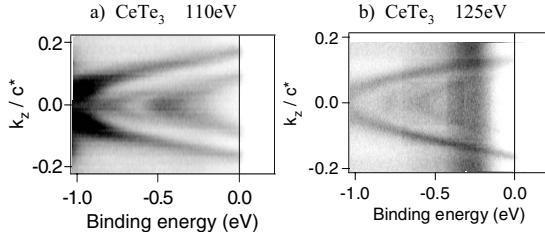


FIG. 7. Comparison of the electronic structure, measured at  $T = 20$  K and  $k_x = 0.6a^*$ , in  $\text{CeTe}_3$  at a photon energy of (a) 110 and (b) 125 eV, i.e., off and on the Ce  $4d$ - $4f$  resonance, respectively. The two parabolas come from the main and folded outer Te bands (see Fig. 8); the line at  $-0.28$  eV in (b) is attributed to the spin-orbit satellite of the Ce resonance.

model, this corresponds to  $t_{\text{para}} = -1.7 \pm 0.15$  eV, a value that corroborates our previous estimation. The variation expected as a function of lattice parameter in the previous paragraph ( $t_{\text{para}} = -1.7$  to  $-1.85$  eV) is shown in Fig. 6(b) to be within the error bar of the measurement. Let us note that the dispersion is defined here over a rather large energy scale and this analysis does not exclude possible renormalization effects near the Fermi level.

### C. Deviations from the tight-binding model

#### 1. Ce contribution

The smooth changes in the electronic structure as a function of rare earth are a good indication that they do not play an active role in the electronic properties. However, it would be interesting to clarify the relationship between the localized  $4f$  moments on the rare earth and the Te band even if their coupling is weak. We present here the results for  $\text{CeTe}_3$ , for which the magnetic susceptibility indicates localized moments of  $2.4\mu_B$ , consistent with trivalent Ce that order antiferromagnetically at  $T_N = 2.8$  K.<sup>22,31</sup> There is a mild upturn of the resistivity below 10 K, suggesting a weak Kondo behavior.<sup>22</sup>

In  $\text{CeTe}_3$ , we observe a nondispersive line at  $E = -0.28$  eV throughout the whole BZ. In Fig. 7, we show that it is strongly enhanced at the Ce  $4d$ - $4f$  transition (120 eV), indicating that it has Ce character. This line is indeed absent in other  $R\text{Te}_3$  systems. It does not interact strongly with Te bands, as there is no detectable perturbation of the Te dispersion at their crossings.

Generally, one would expect a two peak structure for the Ce spectrum, corresponding to screened and unscreened final states of the hole created through the photoemission process ( $4f^1$  and  $4f^0$ , respectively).<sup>32</sup> Their positions and relative intensities are very sensitive to the nature of the coupling between localized moments and the metallic band. Such two peaks were observed in  $\text{CeTe}_2$  at  $-4$  ( $4f^0$ ) and  $-1$  eV ( $4f^1$ ),<sup>33</sup> which is typical of a localized  $\text{Ce}^{3+}$  in a nearly insulating medium. In  $\text{CeTe}_3$ , the  $4f^1$  peak moves closer to the Fermi level ( $-0.28$  eV) and we did not resolve the  $4f^0$  peak from other Te bands at lower binding energies. The  $4f^1$  peak is known to exhibit a spin-orbit splitting of 0.28 eV between  $4f^1_{7/2}$  and  $4f^1_{5/2}$  states. This suggests that the satellite line we

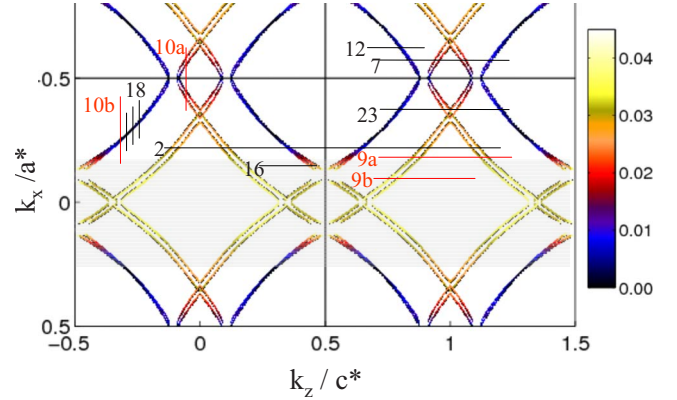


FIG. 8. (Color online)  $\text{LuTe}_3$  FS calculated with the LMTO method. The gray and/or color scale indicates the amplitude of bilayer splitting. The shaded area corresponds to the part of FS gapped by CDW. The red lines correspond to cuts used to give example of bilayer splitting in Figs. 9 and 10. Other lines correspond to cuts shown throughout this paper in figures with number as indicated.

observe is, in fact, the  $4f^1_{5/2}$  spin-orbit satellite of a  $4f^1_{7/2}$  peak centered at the Fermi level, but having a negligibly small intensity.<sup>34</sup> This is the situation expected at temperatures higher than the Kondo temperature  $T_K$ .<sup>32</sup> As this measurement was done at  $T = 20$  K, this result corroborates the idea that  $\text{CeTe}_3$  is a weak Kondo system, with  $T_K \ll 20$  K.

#### 2. Bilayer splitting

One thing neglected in the TB model is the coupling between the Te planes, which gives rise to the bilayer splitting (see Fig. 2). Figure 8 shows the FS of  $\text{LuTe}_3$  obtained with the LMTO method.<sup>35</sup> The shaded area corresponds to the gapped area. The amplitude of the bilayer splitting is indicated as gray scale. It changes quite strongly along the FS, it is larger in the square ( $\delta = 0.03c^*$ ) than in the outer part (typically less than  $\delta = 0.01c^*$ ). The typical full widths of our spectra at half maximum are found between 0.02 and  $0.03c^*$ . Consequently, bilayer splitting is usually not resolved on the outer Fermi surface (except near the corners) but it is in the square. In Figs. 9 and 10, we give examples of the typical line shapes observed in these two parts.

In the square, we typically observe two lines reaching for  $E_F$ ; Fig. 9 gives two examples at different heights in the square, one metallic [Fig. 9(a)] and one gapped [Fig. 9(b)]. They form a sort of inverted V-like shape that is tempting to attribute to the bilayer splitting, although, in the calculations, the two lines are more parallel, at least near  $E_F$ . The relative intensities of the two lines are very sensitive to the photon energy; they are quite different at 55 eV [Fig. 9(a)] but nearly equal at 35 eV [Fig. 9(b)]. Such oscillations in the intensity of bilayer split bands with photon energy were also observed in the well studied case of  $\text{Bi}_2\text{Sr}_2\text{CaCu}_2\text{O}_{8+\delta}$ .<sup>36</sup> The curvature of the outside band seems to be due to the crossing with the folded band at  $-0.8$  eV (see also Fig. 2), but it appears more pronounced experimentally [especially in Fig. 9(a)].

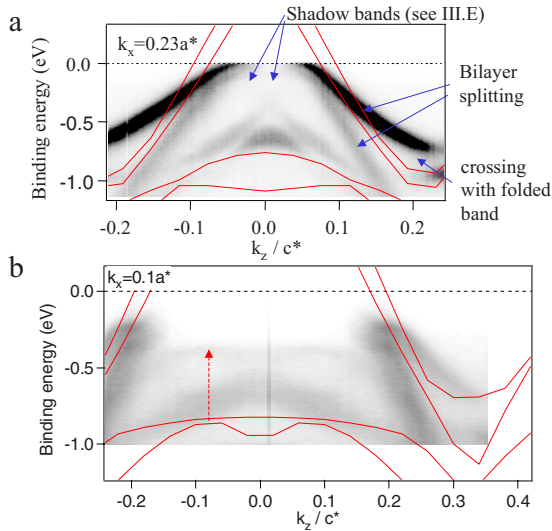


FIG. 9. (Color online) Near  $E_F$  band structure in the square. (a) Measured in  $\text{CeTe}_3$  with photon energy of 55 eV at  $k_x=0.23a^*$  and (b) in  $\text{TbTe}_3$  with 35 eV and  $k_x=0.1a^*$ . The lines are calculated LMTO dispersions.

Other bands are present within the square corresponding to different Te orbitals. The agreement with the calculation is not as good as for the near  $E_F$  bands, which is probably a consequence of the approximations used in the local density. We frequently observe shifts of deep Te bands to lower binding energies. This is the case in Fig. 9(b), where a band with a distinctive two lobe structure seems pushed along the dotted arrow by about 0.5 eV. These shifts seem common, as a similar trend was reported in  $\text{LaTe}_2$ .<sup>37</sup>

Figure 10 shows a typical situation for the outer FS. Near the corner ( $k_z=0$ ), the bilayer splitting is maximum. In Fig. 10(a), the two lines are well resolved, they have almost the same intensity because the photon energy is 35 eV, and the bilayer splitting is  $0.025a^*$  near  $E_F$ . At higher  $k_z$ , the bilayer splitting rapidly decreases and is not resolved anymore along most of the outer FS, as shown in Fig. 10(b) for  $k_z=0.32c^*$  (see position in Fig. 8). The linewidth of the main line here is  $\delta v=0.025a^*$ , indeed quite larger than the calculated splitting at this position,  $\delta=0.005 \pm 0.002a^*$  (the error bar includes differences depending on the details of the calculation). It is also unlikely that this width is dominated by the bilayer splitting, as the lines are not narrower when it is resolved, as in the square [ $\delta v=0.024c^*$  in Fig. 9(a)] or the outer corner [ $\delta v=0.035a^*$  in Fig. 10(a)].

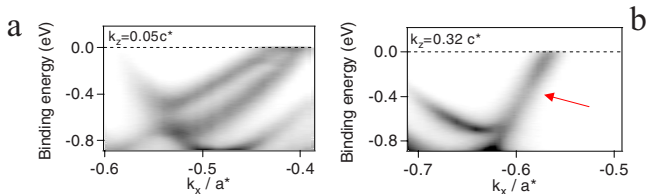


FIG. 10. (Color online) Near  $E_F$  band structure along the outer FS measured in  $\text{YTe}_3$  in the second BZ (see Fig. 8) at 35 eV for (a)  $k_z=0.05c^*$  and (b)  $k_z=0.32c^*$ .

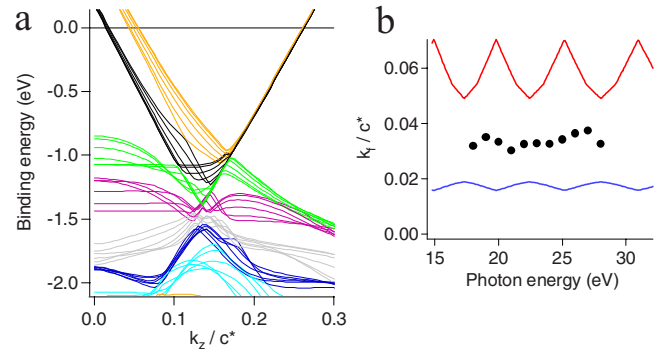


FIG. 11. (Color online) (a) Calculated band dispersion at  $k_x=0.3a^*$  for different  $k_y$  values. (b) Black points:  $k_F$  position measured in  $\text{CeTe}_3$  for the square as a function of photon energy. Solid lines: perpendicular dispersion expected theoretically on the square for the red and blue bands of panel (a).

### 3. Two dimensional character

An interesting issue is the strength of the 3D couplings in these quasi-2D systems, which we have implicitly neglected so far. Although the transport anisotropy is large, these systems remain metallic along the  $b$  axis,<sup>16,22</sup> implying sizable hybridization in the perpendicular direction. 3D couplings often complicate the analysis of the photoemission spectra and might be responsible for a residual broadening of the spectra.<sup>38</sup> Their order of magnitude is therefore important to evaluate.

Figure 11(a) shows the dispersion of Fig. 2 calculated for different values of  $k_y$ . The value of  $k_\perp$  in an ARPES measurement is not known precisely because it is not conserved at the surface crossing. It depends on the photon energy  $E_{\text{ph}}$ ; at the  $\Gamma$  point,  $k_\perp=2m/\hbar^2\sqrt{E_{\text{ph}}+V_0}$ , where  $V_0$  is an inner potential adjusted experimentally.<sup>39</sup> One can therefore expect a line to *shift* and/or *broaden* as a function of the photon energy on the energy scale of the perpendicular dispersion. The relative amount of broadening and shift will depend on the lifetime of the photoelectron in the final state.<sup>38</sup> Indeed, the linewidth can be written in simple cases as  $\delta v=\Gamma_i+v_{i\perp}/v_{f\perp}\Gamma_f$ , where  $\Gamma_i$  and  $\Gamma_f$  are the lifetimes in the initial and final states and  $v_{i\perp}$  and  $v_{f\perp}$  are the slopes of the perpendicular dispersion in each state.<sup>40</sup> One is typically interested in  $\Gamma_i$ , but it is usually masked by the larger  $\Gamma_f$  (the final state having a much higher energy of the order of the photon energy), unless  $v_{i\perp}$  is very small.

For the outer bands, the dispersion is fairly independent of  $k_y$ , as expected for a good 2D metal. The total spread of  $k_F$  as a function of  $k_y$  is  $\delta_{3D}=9.10^{-4}c^*$  and  $\delta_{3D}=2.10^{-4}c^*$ , for the two split bands, obviously totally negligible compared to the width of  $\delta v=0.02-0.03c^*$ . The perpendicular dispersion is larger in the square, as could already be anticipated from the larger bilayer splitting, indicative of stronger transverse couplings. Figure 11(b) displays the variations of  $k_F$  expected theoretically for the red and blue bands forming the square (solid lines). They are plotted as a function of photon energy, assuming a typical value  $V_0=10$  eV (Refs. 38 and 39) in the previous formula of  $k_\perp$ . They are compared to the  $k_F$  values measured in  $\text{CeTe}_3$  at different photon energies (black points). Note that the bilayer splitting is not resolved in the

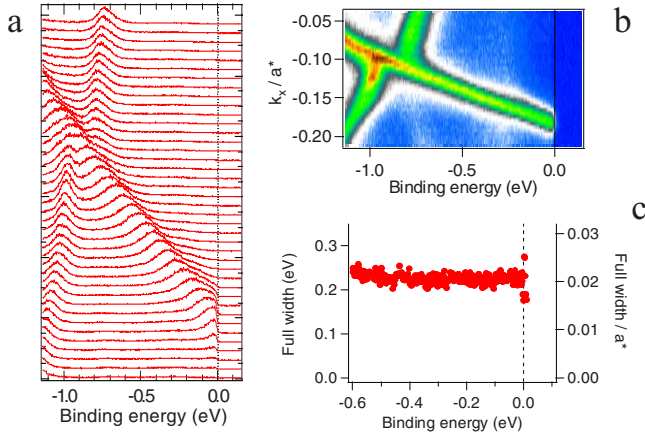


FIG. 12. (Color online) Line shape analysis in CeTe<sub>3</sub> at 55 eV and 20 K for a cut of the outer FS at  $k_x=0.62c^*$ . (a) EDC stacks. (b) Image plot. (c) Full width at half maximum of MDC spectra (the value in energy is obtained by multiplying with the slope of dispersion).

square near  $E_F$  [Fig. 9(a)]. We do not observe oscillations in the position measured for  $k_F$  and the variation is less  $0.007c^*$ . Although the linewidth is of the same order of magnitude as the calculated perpendicular dispersion for the red band, it is unlikely that it is dominated by  $\Gamma_f$ , since the linewidth is very similar for the outer band, where  $v_{i\perp}$  is reduced by a factor 20. We conclude that there is no obvious contribution of 3D couplings detectable in our spectra.

**D. Spectral line shape**

Because of its simple, well understood, and nearly 2D electronic structure,  $R\text{Te}_3$  offers a favorable situation to extract detailed information about the electronic self-energy from the ARPES line shape.<sup>36,39</sup> Since examples of “simple” low dimensional systems are rare, this deserves attention. Figure 12 exemplifies typical line shapes along the outer FS, where the band is well separated from other bands, the bilayer splitting is minimum, and the 3D couplings are negligible. They have low backgrounds both for cuts taken at momentum distribution curve (MDC) and constant energy distribution curve (EDC), which is another advantage for line fitting. Yet, the linewidth [Fig. 12(c)] appears rather large and does not exhibit a significant decrease near  $E_F$ , which would be the fingerprint of a Fermi liquid.<sup>41,42</sup> We note, however, that the Fermi step is very well defined (see also Fig. 21), so that this case is completely different from that of a “bad metal,” where broad lines are associated with a low weight at the Fermi level, due to strong correlations, low dimensionality, and/or polaronic effects.<sup>5</sup> It is worth emphasizing this point because the opening of the CDW gap along  $c^*$  gives an effective 1D character to the problem, which raises the question of possible 1D features in the physics of  $R\text{Te}_3$ . A power law behavior of the optical conductivity was recently attributed to the formation of a Tomonaga–Luttinger liquid.<sup>23</sup> We do not observe equivalent effects in the ARPES line shapes.

The behavior of the width in Fig. 12 is typical of that found in all  $R\text{Te}_3$  systems we have investigated. Most of the

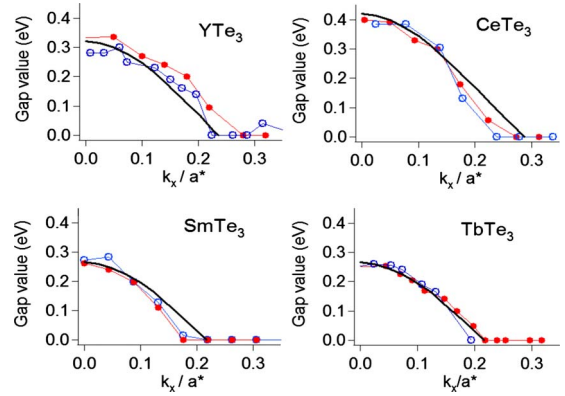


FIG. 13. (Color online)  $k$  dependence of the gap along the Fermi surface for the square part of FS (solid red circles) and outer part (open blue circles).  $k_x$  is used as implicit parameter for the position on FS. The black line describes the decrease in the gap expected because of the imperfect nesting away from  $k_x=0$  (see Sec. III D).

changes we observed as a function of binding energy could ultimately be attributed to crossings with other lines (such as the Ce satellite at  $-0.28$  eV) or weak CDW shadow bands (red arrow in Fig. 10(b); see Sec. III B). The MDC linewidths are comprised between  $\delta v_a=0.03$  and  $0.05 \text{ \AA}^{-1}$  for different samples and/or different cleaves. This translates to a rather large energy width for EDC spectra ( $\delta v_e = \delta v_a^* V_s = 0.2-0.3$  eV, where  $V_s$  is the slope of the dispersion), but this is essentially due to the fact that  $V_s$  is about 1 order of magnitude larger here than in many reference systems, such as cuprates<sup>36</sup> or  $1T\text{-TiTe}_2$ .<sup>42</sup>

If taken at face value, the MDC width would correspond to a mean free path  $l=2/\delta v_a=40-60 \text{ \AA}$ , which seems rather small for these good metals where quantum oscillations have been observed.<sup>43</sup> As transport and ARPES lifetimes are different, this comparison is only qualitative. We have seen that the bilayer splitting and 3D couplings should be rather negligible contributions on this scale. On the other hand, the angular resolution was usually set to  $\delta k_{\text{res}}=0.3^\circ$ , which is smaller but not negligible compared to these linewidths (it corresponds to  $0.02 \text{ \AA}^{-1}$  at 50 eV). For these systems with large Fermi velocities, the angular resolution is indeed a much stronger constraint than energy resolution ( $\delta E_{\text{res}}$  was typically 10–20 meV, much smaller than  $V_s \cdot \delta k_{\text{res}}$ ). We did not observe a large improvement when using a higher resolution mode of the analyzer ( $0.1^\circ$ ), which rules out that it is entirely a resolution problem. We believe that other types of extrinsic angular broadening could be an issue, for example, a distribution of angles at the sample surface. Although these samples cleave very well, giving smooth and shiny surface, they often exhibit curved surfaces, which could limit our effective resolution. ARPES experiments with ultrasmall spot may be able to clarify this issue. Alternatively, impurities at the surface could reduce the mean free path we measure.

**III. CHARGE DENSITY WAVE PROPERTIES**

Figures 13 and 14 summarize the main results of our

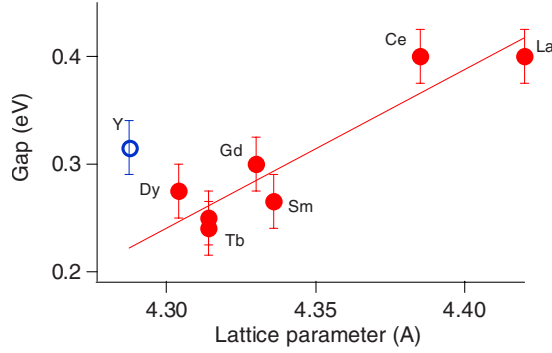


FIG. 14. (Color online) Maximum gap value for different rare earths and  $\text{YTe}_3$  (open circle) plotted as a function of the lattice parameter  $c$ . The straight line is a guide for the eyes.

ARPES investigation of the  $\text{RTe}_3$  CDW properties. The evolution of the gap in  $k$  space is shown in Fig. 13 for different compounds. We find identical gaps on the square and outer FS pieces for a given  $k_x$  value; therefore, the gap is plotted as a function of  $k_x$ . The gap is maximum at  $k_x=0$  and decreases to zero for a value  $k_x^0$  comprised between 0.18 and  $0.28a^*$ . This qualitative behavior is the same for all rare earth we have studied (Dy, Tb, Gd, Sm, Ce, La) and Y. On the other hand, there are significant quantitative changes in the maximum gap value and in  $k_x^0$  as a function of  $R$ . Figure 14 displays the maximum gap value as a function of the lattice parameter. It is defined with respect to the leading edge of the spectra (see Sec. III D). In  $\text{SmTe}_3$ , our value (280 meV) corresponds well to the 260 meV first measured by Gweon *et al.*<sup>20</sup> The increase is roughly linear as a function of lattice constant, with maybe an exception for  $\text{YTe}_3$ , which is the only non-rare-earth compound.

The change in the gap along the FS is an essential feature to understand the origin of the CDW. We will show that the model of a nesting driven sinusoidal charge density wave allows us to explain in detail the location of the gap in  $k$  space (Sec. III D). This model also implies the presence of metallic pockets and shadow bands in the regions that are not perfectly nested, which we observe and discuss in Sec. III E. The increase in the gap with lattice parameter is another way to investigate the nature of the CDW. The CDW results from a compromise between the loss of elastic energy in the distortion and the gain of electronic energy (see Sec. III F). The basic idea is that the larger  $n(E_F)$  caused by the lattice expansion increases the gain of electronic energy when a gap opens and then stabilizes the CDW.<sup>14</sup> We give a quantitative discussion of this phenomenon, which leads to the estimation of the important CDW parameters, such as the electron-phonon coupling and the relevant phonon frequencies.

#### A. Interacting band structure in the charge density wave state

We introduce here a simple theoretical model to describe the modification of the band structure in the CDW state. The electron-phonon coupling responsible for the CDW is described by the following Hamiltonian:

$$H = \sum_k \varepsilon_k c_k^\dagger c_k + \sum_{k,q} g_q c_{k+q}^\dagger c_k (a_q + a_{-q}^\dagger),$$

where  $g_q$  is the electron-phonon coupling strength for the wave vector  $q$  and  $c_k^\dagger$  ( $c_k$ ) are the creation (destruction) op-

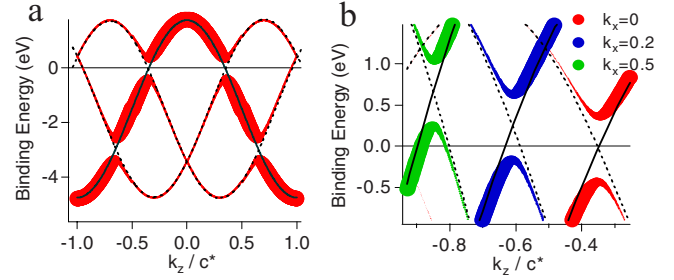


FIG. 15. (Color online) (a) Points (red online): sketch of the dispersion in the CDW state at  $k_x=0$ , calculated for  $V=0.4$  eV and  $q_{\text{CDW}}=0.32c^*$ . The size of the points is proportional to the spectral weight  $|u_k|^2$  (see text). The solid black line is the original dispersion from the TB model, dotted lines are translated by  $c^* \pm q_{\text{CDW}}$ . (b) Zoom near the Fermi level for the same calculation and different  $k_x$  values.

erators for electrons and  $a_q^\dagger$  ( $a_q$ ) for phonons.

In the CDW state, a static distortion takes place for a wave vector  $\pm q_{\text{CDW}}$ , implying  $\langle a_{\pm q} \rangle = \langle a_{\pm q}^\dagger \rangle \neq 0$  at this wave vector. This creates a coupling  $V=2g_{q_{\text{CDW}}} \langle a_{q_{\text{CDW}}} \rangle$  between states  $|k\rangle$  and  $|k \pm q_{\text{CDW}}\rangle$ . Another wave functions allowing for the admixture of these states have to be defined with the form

$$|\psi_k\rangle = u_{k-q_{\text{CDW}}} |k - q_{\text{CDW}}\rangle + u_k |k\rangle + u_{k+q_{\text{CDW}}} |k + q_{\text{CDW}}\rangle$$

where the coefficients are the solutions of the matrix

$$\begin{bmatrix} \varepsilon_{k-q_{\text{CDW}}} & V & 0 \\ V & \varepsilon_k & V \\ 0 & V & \varepsilon_{k+q_{\text{CDW}}} \end{bmatrix}.$$

Here, we truncate the interaction at the first harmonic, although, in principle, all harmonics  $n \cdot q_{\text{CDW}}$  should be included.

The dispersion of these wave functions is shown in Fig. 15(a), with a size of the markers chosen as  $|u_k|^2$ . Wave functions are essentially unchanged away from the crossings between  $|k\rangle$  (solid line) and  $|k \pm q_{\text{CDW}}\rangle$  (dotted lines), i.e.,  $u_k = 1$  or 0. At the crossing, a gap with amplitude of  $2V$  opens and some weight is distributed on the translated parts of the band structure (dotted lines), which are called the *shadow bands*. Their intensity is proportional to  $V$  and decreases very fast away from the crossing. This is better seen in Fig. 15(b), where the part near the Fermi level is emphasized.

An example of the typical resulting shape of the dispersion in the gapped state is shown in Fig. 16. The band “turns away” from the Fermi level after reaching a maximum, corresponding to the gap value (here 330 meV) and its intensity rapidly vanishes. The observation of such a shape is, in fact, the best proof that the band is indeed gapped versus its intensity would be accidentally reduced near  $E_F$  by matrix element effects. In Fig. 16(b), we display its intensity as a function of the distance with respect to the crossing between the main and translated bands. The qualitative variation of this intensity is in good agreement with the expectations of the theoretical model. Two theoretical variations are given

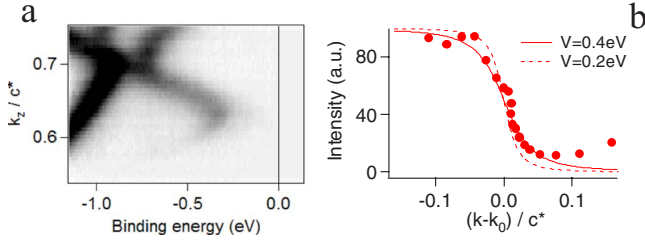


FIG. 16. (Color online) Shadow band in the gapped state. (a) Band from the outer FS, measured along  $k_z$  at  $k_x=0.1a^*$  in CeTe<sub>3</sub>. (b) Red points: intensity of this band as a function of  $k$  (zero is the position of the crossing). It is extracted by a fit of the EDC spectra with a Gaussian and a parabolic background. Theoretical variation for this weight is also shown for  $V=0.4$  eV (as solid line) and  $V=0.2$  eV (as dotted line).

for  $V=0.4$  eV (solid line) and  $V=0.2$  eV (dotted line). However, a quantitative comparison remains difficult because, in many cases, the photoemission intensity is modulated by matrix element effects that partially mask the intrinsic variation.

Figure 15(b) summarizes the evolution expected as a function of the degree of nesting of the FS. When the FS is perfectly nested, the crossing takes place by definition at the Fermi level. The gap measured by ARPES with respect to  $E_F$  is maximum and equals  $V$ . This is the case for  $k_x=0$  represented in red on Fig. 15(b). When the perfect nesting is lost ( $k_x > 0$ ), the crossing takes place above  $E_F$  and the apparent gap at  $E_F$  decreases (see  $k_x=0.2$ ). Eventually, when the crossing takes place at an energy higher than  $V$  above  $E_F$ , the band crosses again the Fermi level and remains metallic (see  $k_x=0.5$ ). In this case, two crossings should, in fact, be observed at  $E_F$ , with large and small weights, forming the two sides of a metallic pocket. These theoretical pockets are shown in Fig. 17 for the simplified case of an isolated  $p_x$  band. The side with large weight follows the original FS and the other side the FS translated by  $c^* \pm q_{CDW}$ . Note that we use here the usual definition of  $q_{CDW}$  in the 3D BZ, which, in fact, nests the main and folded FS (see Fig. 4). We, however, show translated bands by  $c^* \pm q_{CDW}$ , which is equivalent but connects bands from the same Te plane. The extension of the metallic pocket sensitively depends on the strength of the gap; it is shown for  $V=0.2$  eV in Fig. 17(a) and  $V=0.4$  eV in Fig. 17(b).

### B. Value of the interaction parameter $V$

In the case represented in Fig. 17, the CDW vector has been chosen, so that the original FS and its translated exactly overlap on the corner of the square. In the corresponding band structure (Fig. 15), the Fermi level at  $k_x=0$  lies in the middle of the full interacting gap of  $2V$ . However, as ARPES only measures occupied states, one cannot directly observe this full interacting gap and this leaves an ambiguity on the size of  $V$ . When  $k_x$  increases, the symmetry is such that the crossing between the main and translated bands always takes place *above* the Fermi level [Fig. 15(b)], so that the full interacting gap is still eluding measurement.

A closer inspection of Fig. 17 reveals another type of crossing between main and translated bands, indicated by a

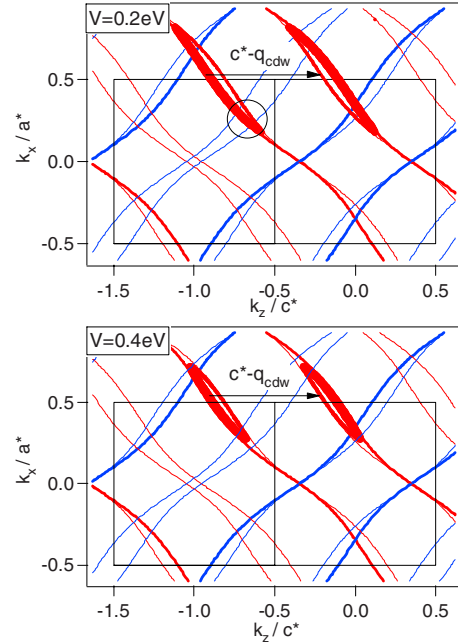


FIG. 17. (Color online) Metallic pockets from the  $p_x$  band expected after CDW reconstruction for the two different values of  $V$ . The interaction with  $p_z$  is neglected. The thick red and blue lines correspond to original FS for  $p_x$  and  $p_z$ . Thin lines are FS translated by  $c^* + q_{CDW}$  or  $c^* - q_{CDW}$ . The size of the markers is proportional to the spectral weight.

circle. These bands belong to different orbitals; they do not nest the original FS, but they link  $|k\rangle$  and  $|k+q_{CDW}\rangle$  electrons, and are therefore also subject to the interaction  $V$ . Their crossing turns out to take place below  $E_F$ , which allows us to directly measure  $2V$ . Indeed, we see that these bands interact with each other in our data, as shown in Fig. 18. In Fig. 18(a), a strong “break” is observed in the dispersion of LaTe<sub>3</sub> at a position corresponding well to that expected for such a crossing. The shadow band intensity is, however, so weak that one could not guess that there is a crossing there without the TB simulation. The line shape is detailed in Fig. 18(b), showing the opening of a break with peak-to-peak distance  $2V=0.37$  eV. The same behavior is observed for YTe<sub>3</sub> in Fig. 18(c) [the same data as Fig. 10(b)]. Interestingly, the break is smaller in this case ( $2V=0.21$  eV). This is consistent with the smaller gap in YTe<sub>3</sub> ( $\Delta_{max}=0.33$  eV) than in LaTe<sub>3</sub> ( $\Delta_{max}=0.4$  eV). On the other hand, we observe here  $\Delta_{max} \gg 2V$  rather than  $\Delta_{max}=V$  expected in Fig. 15.

One would obtain  $\Delta_{max}=2V$ , if the Fermi level at  $k_x=0$  was set at the top of the gap rather than in its middle. Figure 19 compares the band structure at  $k_x=0$  for the two scenarios:  $\Delta_{max}=V$  [Fig. 19(a)] and  $\Delta_{max}=2V$  [Fig. 19(b)]. In the second case,  $q_{CDW}$  is chosen a little longer to allow the main band and its translated to cross at  $-V$ . As shown in Figs. 19(c) and 19(d), the gap observed at the Fermi level by ARPES as a function of  $k_x$  would be very similar, although  $V$  would be different by a factor 2.

One important difference between these two scenarios concerns the *conservation of the number of occupied states*. For the common case of a homogeneously gapped FS,  $E_F$  has

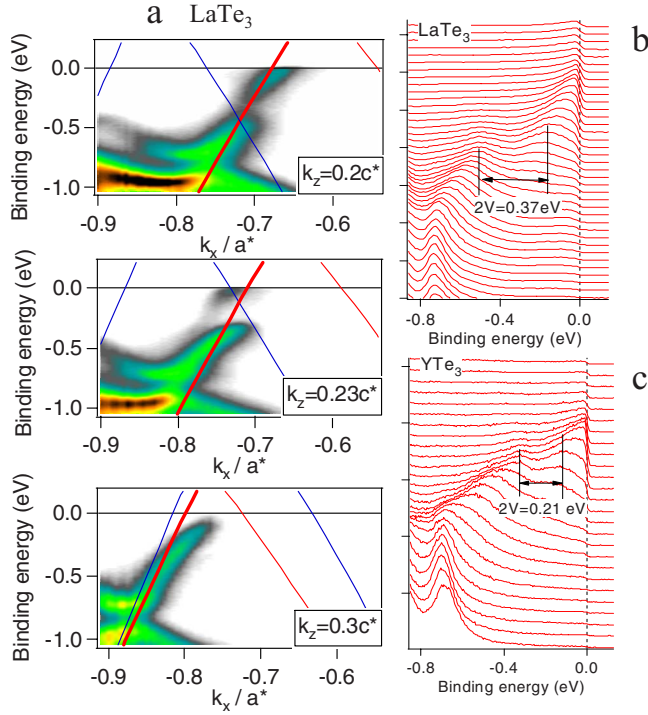


FIG. 18. (Color online) (a) Dispersion along the outer FS in  $\text{LaTe}_3$  for three  $k_z$  values ( $h\nu=35 \text{ eV}$ ). The TB  $p_x$  band is shown as a thick red line and CDW shadow bands as thin lines. (b) Detail of the dispersion in  $\text{LaTe}_3$  at  $k_z=0.2c^*$ . (c) Equivalent situation for  $\text{YTe}_3$  at  $k_z=0.32c^*$  [Fig. 10(b)].

to be in the middle of the gap to conserve the number of electrons. However, the situation is quite different here because of the imperfect nesting. As soon as the crossing between the original band and its translated band takes place away from the Fermi level, there is a different number of

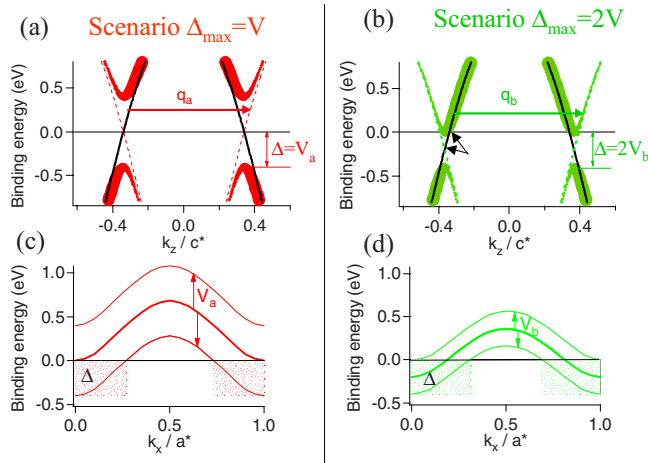


FIG. 19. (Color online) [(a) and (b)] The black line is the TB band at  $k_x=0$ ; dotted lines are translated by  $\pm q$ , with  $q_a=0.68c^*$  and  $q_b=0.733c^*$ . The CDW interaction parameter  $V$  is chosen to get the same gap in the two cases:  $V_a=0.4 \text{ eV}$  and  $V_b=0.2 \text{ eV}$ . [(c) and (d)] The thick line is the position of the crossing between the original and translated bands as a function of  $k_x$  for the values of  $q$  and  $V$  corresponding to (a) and (b). Thin lines are translated by  $\pm V$ . Dotted areas represent the gapped regions.

occupied states in the gapped and metallic state. In the case of Fig. 19(b), for example, the states above the crossing position (this region is delimited by the black arrows) were occupied in the metallic state but are empty in the CDW state (the weight in the shadow band is just shifted from the main band, so that this does not change the counting of occupied states). This roughly corresponds to a loss of  $V/V_F * n(k)$  states, with  $n(k)$  being the density of  $k$  states,  $V_F$  the Fermi velocity, and  $V$  the CDW interaction parameter. More generally, the imbalance is just proportional to the position of the crossing in energy. It is easy to see in Fig. 19(d) that the loss of states near  $k_x=0$  will be compensated by a gain of states for higher  $k_x$ . On the contrary, in Fig. 19(c), there is no such compensation and there would be a significant excess of electrons in the CDW state, which is obviously not self-consistent and requires a shift of  $E_F$ . Direct calculations of the density of states in metallic and gapped states (see Sec. III F) show that the Fermi level moves very close to the position of scenario (b) to conserve the number of electrons. This also maximizes the gain of electronic energy for a given value of  $V$ . This gives a natural explanation for the choice of the situation  $\Delta_{\max} \gg 2V$  observed in Fig. 18.

In principle, probes that also measure unoccupied states, such as STM, could directly confirm or infirm this scenario. However, they are not  $k$  resolved and, as there is a large distribution of gaps, the analysis is not straightforward.<sup>19</sup>

### C. Value of $q_{\text{CDW}}$

Another consequence of scenario (b) is that  $q_{\text{CDW}}$  should change with  $V$ . This is an interesting point as a change in  $q_{\text{CDW}}$  is indeed observed experimentally. In scenario (a),  $q_{\text{CDW}}$  is fixed by the size of the FS to  $2k_F=0.68c^*$  at  $k_x=0$  (in the 3D BZ,  $q_{\text{CDW}}=1-2k_F=0.32c^*$ ). As seen in Sec. II A, this size should not and does not change with  $R$ . On the contrary, in scenario (b),  $q_{\text{CDW}}$  is chosen for the crossing to take place at  $-V$  for  $k_x=0$  and therefore systematically changes with  $V$ .

Satellite positions were observed by transmission electron microscopy (TEM)<sup>14</sup> to increase from  $q_{\text{CDW}}=0.27c^*$  (for  $c \approx 4.4 \text{ \AA}$ ) to  $0.31c^*$  (for  $c \approx 4.3 \text{ \AA}$ ). Our recent x-ray measurements find the satellites at  $q_{\text{CDW}}=0.296c^*$  in  $\text{TbTe}_3$  ( $a=4.312 \text{ \AA}$ ).<sup>18</sup> We report in Fig. 20 the values we measured for different rare earths.<sup>18</sup> To obtain a crossing at  $E=-V$  for  $k_x=0$ , one gets from the TB model

$$1 - q_{\text{CDW}} = \frac{2}{\pi} \arccos \left( \frac{V - E_F}{2(t_{\text{para}} + t_{\text{perp}})} \right).$$

Figure 20 illustrates the changes in  $q_{\text{CDW}}$  expected in this scenario for the two extreme values of  $t_{\text{para}}$  determined in Sec. II. The change with  $t_{\text{para}}$  is negligible in front of that with  $V$ . The agreement with the experimental data is quite spectacular, although the absolute values are slightly larger. This supports this model as the basic origin of the variation of  $q_{\text{CDW}}$ . Indeed, there is no variation of  $q_{\text{CDW}}$  with  $R$  expected from our study of the nesting properties of the FS in  $R\text{Te}_3$ . If small variations exist as a function of  $R$ , they have to be restricted to the error bar of  $t_{\text{perp}}$  or to subtle changes in bilayer splitting, perpendicular couplings, or interaction between  $p_x$  and  $p_z$  (arising, for example, from slightly different

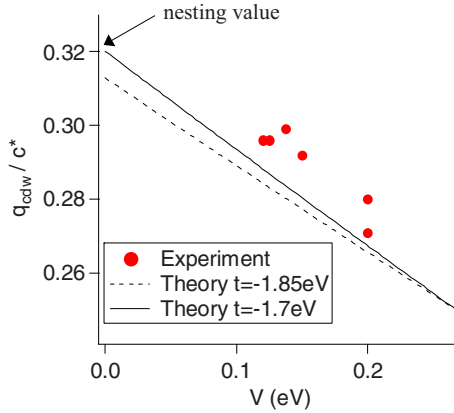


FIG. 20. (Color online) Points: experimental values of  $q_{\text{CDW}}$  measured by x ray (Refs. 18 and 17 for  $\text{CeTe}_3$ ) as a function of  $V = \Delta/2$  ( $\Delta$  is taken from Fig. 14). Black lines: theoretical variation for  $q_{\text{CDW}}$  as a function of  $V$  (see text) for  $t_{\text{para}} = -1.7$  eV and  $t_{\text{para}} = -1.85$  eV.

orthorhombicities). Such effects are probably important for a complete description of the CDW. The existence of the two successive transitions in heavy rare-earth compounds<sup>18</sup> or the deviation of  $\text{YTe}_3$  from the general trend of  $\text{RTe}_3$  (Fig. 14) is a proof that there are subtleties not captured by the TB model. However, they are probably not able to overcome the strong trend exposed in Fig. 20.

#### D. $k$ dependence of the gap

We have seen that a variation of the gap along the FS is a natural consequence of the nesting driven CDW, when the FS exhibits imperfect nesting, even when the interaction  $V$  itself is isotropic. Conversely, the distribution of the gap over the FS directly informs about the direction of the nesting. For example, the CDW wave vector has to be parallel to  $c^*$  to explain the opening of the same gap on the square and outer FS at one  $k_x$  value (Fig. 13). Such a direction is fully consistent with x-ray and TEM studies.<sup>14,17,18</sup> We have also already seen that the experimental values of  $q_{\text{CDW}}$  closely correspond to the best FS nesting wave vector.

We now study the  $k$  dependence of the gap quantitatively. Figure 21(a) gives examples of leading edge spectra in  $\text{SmTe}_3$  at different  $k_x$  values used to determine the gap in Fig. 13. The Fermi edge [black line on Fig. 21(a) with a width of 30 meV, corresponding to the experimental resolution] is very clear, making the determination of the metallic zones unambiguous. When the gap opens, the Fermi edge is preserved, but a double step is commonly found, especially on the outer part. We believe that, rather than a distribution of gap values, this is due to the bilayer splitting. Figure 21(b) shows data acquired at 35 eV instead of 55 eV in Fig. 21(a) (although in  $\text{LaTe}_3$  instead of  $\text{SmTe}_3$ ). The structure near  $E_F$  resembles a double peak, with two different gaps, rather than a line with shoulder. This could be explained by the variation of intensity of the bilayer split bands with photon intensity described in Sec. II C 2. In all cases, we have aligned the Fermi edge on the more deeply gapped part. We note that slightly different gap values were reported for the two parts

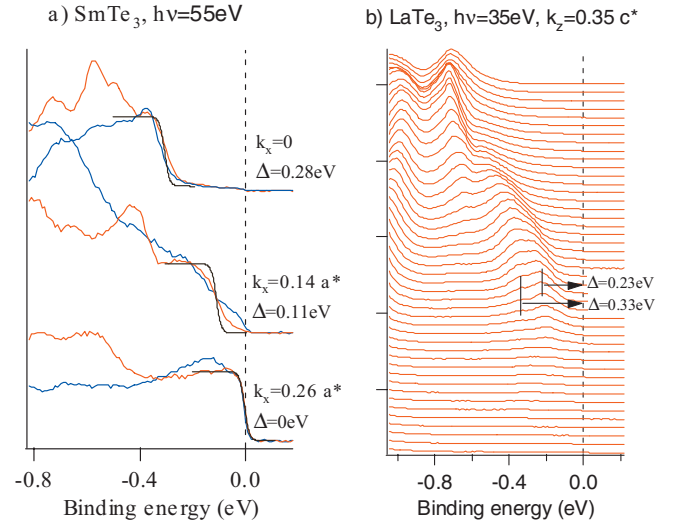


FIG. 21. (Color) (a) Leading edge spectra in  $\text{SmTe}_3$  at different  $k_x$  values and  $h\nu = 55$  eV on square part (red) and outer part (blue). The black line is a fitted Fermi step. (b) EDC spectra on the outer part in  $\text{LaTe}_3$  at 35 eV and  $k_z = 0.35 c^*$ .

at a same  $k_x$  value in Ref. 20. This could be due to a different treatment of this bilayer splitting or to a lower accuracy of this first measurement done only in first BZ, where the intensity of the outer part is very weak. In all investigated cases, we have observed identical gaps on the two parts within the experimental accuracy.

Knowing the value of the CDW wave vector, it is straightforward to deduce the  $k$  dependence of the gap expected within the TB model from the variation of nesting. The principle is that of Fig. 19(d) and can be calculated for any value of  $V$ . We report on Fig. 13 these variations as a black line, with the values for  $q_{\text{CDW}}$  taken from the formula of Sec. III C. The agreement is very satisfying, although the measured gap seems to fall to zero a little faster in the measurement than in the theory. A natural consequence of this simple model is that the position  $k_x^0$  at which the gap becomes zero depends on the maximum gap value. We calculate a linear variation of  $k_x^0$  for a gap between 0.2 and 0.4 eV, which is shown in Fig. 22 and fits well with the experimental values, despite some scattering in the data points. We conclude that the general behavior of the gap opening directly results from the nesting properties of the FS.

#### E. Metallic parts of the electronic structure

A unique feature of  $\text{RTe}_3$  is the possibility of directly observing by ARPES the reconstructed FS, as we have discussed in Ref. 21 and will develop here. Whereas shadow bands are commonly seen in the gapped state<sup>8,13</sup> (like in Fig. 16), they are rarely detectable in metallic situations [like  $k_x = 0.5$  in Fig. 15(b)] because their intensity when they reappear at  $E_F$  is already very small. However, observing these lines gives detailed information about the deviation from nesting and allows us to fully characterize the CDW state.

In Fig. 9(a), shadow bands were visible within the metallic part of the square, although they are rather weak. Figure

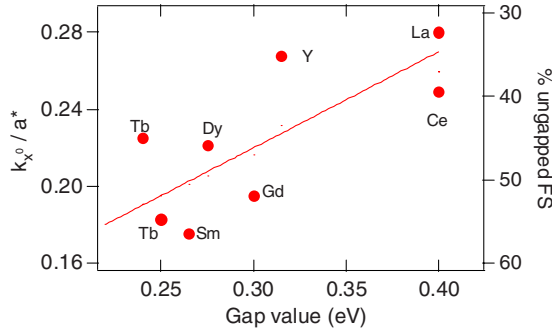


FIG. 22. (Color online)  $k_x$  value at which the gap on FS becomes zero as a function of the maximum gap value. The samples are the same as those in Fig. 9. Straight line is the position of  $k_x^0$  calculated as a function of the gap value in the TB model. The right axis indicates the corresponding fraction of the FS contour that remains metallic.

23 gives two examples of shadow bands near the junction between square and outer parts (see position in Fig. 8) for  $\text{CeTe}_3$  and  $\text{TbTe}_3$ , i.e., for large and small  $V$ . Six bands cross the Fermi level in this area,  $p_x$  and  $p_z$ , their two shadow bands, and their two folded bands. The dotted lines in Fig. 23(a) correspond to the dispersion of  $p_x$  and  $p_z$  in the CDW state (i.e., including the shadow band). Note that for  $\text{TbTe}_3$ , the asymmetry in  $k_z$  is due to a  $7^\circ$  misalignment of the sample. Although weak, the shadow bands are clearly detected. MDC cuts near  $E_F$  [Figs. 23(c) and 23(d)] allow us to estimate their intensity to 12% of the main line in  $\text{CeTe}_3$  and 3% in  $\text{TbTe}_3$ . Theoretically, one expects in this region an 8% at  $V=0.2$  eV and a 3% for  $V=0.14$  eV ( $\text{TbTe}_3$ ), in reasonable agreement with our experimental estimation. Note that these predicted intensities are still quite small, so that it is clear that this work would not be possible without the large gap in  $R\text{Te}_3$ . As shown in Ref. 21, the evolution of the

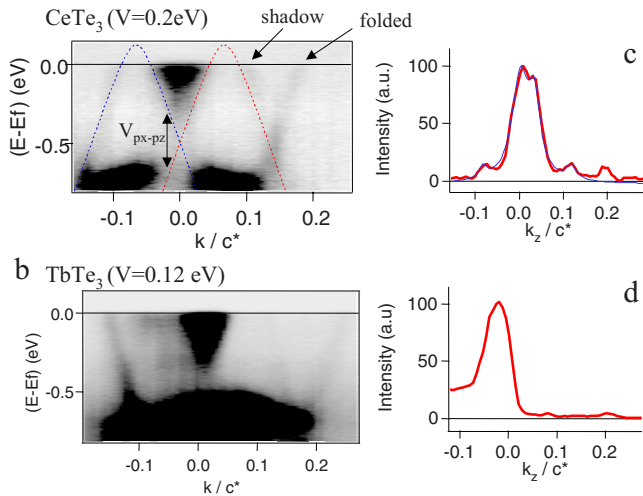


FIG. 23. (Color online) (a) Dispersion in  $\text{CeTe}_3$  along  $c^*$  at  $k_x = 0.38a^*$  and  $h\nu = 55$  eV. The dotted lines are dispersion for  $p_x$  and  $p_z$  in the CDW state. (b) Dispersion in  $\text{TbTe}_3$  along a direction at  $7^\circ$  with respect to  $c^*$  at  $k_x = 0.35a^*$  and  $h\nu = 55$  eV. [(c) and (d)] MDC cut near  $E_F$  corresponding to (a) and (b). In (c), the thin line (blue online) is a three Lorentzians fit.

shadow bands can be followed from  $k_x = 0.3a^*$  up to  $0.45a^*$ , making their assignment unambiguous.

The real shape of the FS can be traced from the crossing position of these main and shadow bands. It is more complicated than in Fig. 17 because of the additional interactions between  $p_x$  and  $p_z$  and with the folded FS. The interaction between  $p_x$  and  $p_z$  is visible in Fig. 23(a); it opens a gap of about  $2V_{px-pz} \approx 0.3$  eV at their crossing, which replaces the linear dispersions near  $E_F$  by a shallow parabola. This is in good agreement with the band calculation (see, for example, Fig. 2, where  $2V_{px-pz} \approx 0.2$  eV). Taking this interaction into account, the FS evolves from the 2D TB FS of Fig. 4(a) to the square and outer sheets of Fig. 4(b) (for clarity, a large  $V_{px-pz} \approx 0.3$  eV is used in this figure). The 3D FS is obtained by folding the 2D with respect to the 3D BZ, as sketched on Fig. 4(c). The main and folded bands also interact. This can be seen in Fig. 2(b), where a gap  $2V_{3D} \approx 0.18$  eV opens at their crossing, which takes place at  $-0.8$  eV. This is a similar strength as for the CDW interaction and, indeed, in Fig. 23, folded bands appear with similar intensity as the CDW shadow bands. After interaction [Fig. 24(a)], the outer part breaks into a small oval pocket near the zone boundary and a larger squared feature. The oval pocket is clearly present in the experimental data [see Fig. 24(c)]. The periodicity is the one of the 3D BZ, but the distribution of the spectral weight is reminiscent of the 2D FS.<sup>21</sup> Once again, we take the size of the markers proportional to the spectral weight.

In Fig. 24, we proceed to the full reconstruction of the FS in the CDW state. This is similar to Fig. 17 but we now use the real FS of Fig. 24(a) instead of that of Fig. 4(a). The main effect is a gapping of a large stripe along  $k_z$  for about  $-0.25a^* < k_x < 0.25a^*$ . The remaining fraction of the square is “closed” at the bottom by the shadow FS. The structure of the top of the square is more complicated. In the case of  $\text{CeTe}_3$  [Fig. 24(c)], it clearly does not close but smoothly connects to the shadow FS. However, this shape sensitively depends on the relative strength of  $V_{px-pz}$  and  $V_q$  and also probably on the bilayer splitting. For  $\text{YTe}_3$  (Fig. 5), the top part of the square is clearly closed. The fact that one can sort out these details is mainly the consequence of much improved resolution and data rate in modern ARPES. To close the other side of the pocket, along the outer part, the mechanism is similar to the one band case of Fig. 17.

One may wonder if the interaction at  $q_{CDW}$  is equivalent to that at  $(c^* - q_{CDW})$ , as we have seen that it is only when the weak folded FS is considered that  $q_{CDW}$  becomes meaningful. If it is, we should observe in our data a gap at the crossing between the folded and CDW shadow bands. On the contrary, it seems in Fig. 23 that these two bands cross *without interacting*. In Fig. 24(b), we calculate the FS in two extreme cases, with  $V(q_{CDW}) = 0 (k_x > 0)$  and  $V(q_{CDW}) = V(c^* - q_{CDW}) (k_x < 0)$ . The crossing between folded and shadow FS is indicated by the black arrows and this region is quite different in the two cases. The comparison with the experimental map of Fig. 24(c) clearly favors the first case.

This is a particularity of the CDW in this system, which is dominated by the in-plane coupling and is, in fact, essentially 2D. If not properly recognized, this could mimic a deviation from a sinusoidal distortion. In Ref. 17, it was proposed that

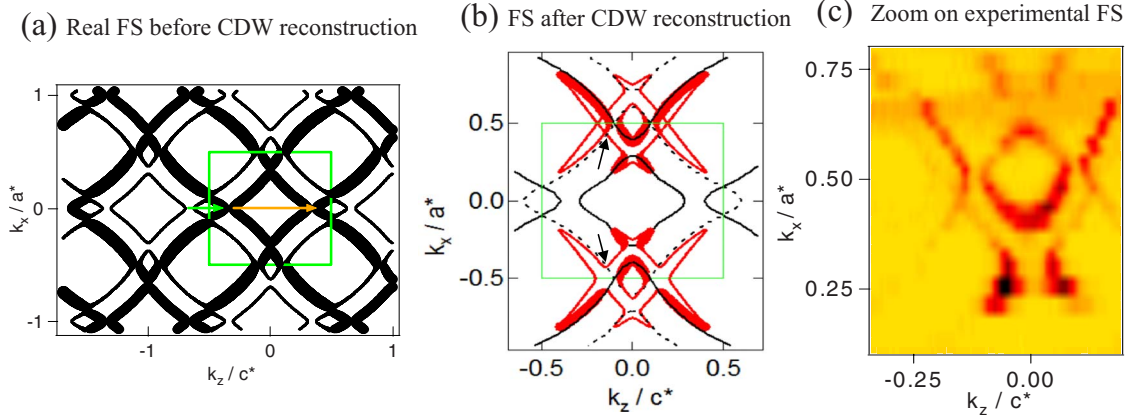


FIG. 24. (Color online) (a) 3D FS including interaction between  $p_x$  and  $p_z$  and between main and folded bands (bilayer splitting is omitted). The green square is the 3D BZ. The size of the markers is proportional to the spectral weight. The red arrows correspond to CDW wave vectors ( $c^*-q_{\text{CDW}}$  and  $q_{\text{CDW}}$ ). (b) Red markers: weight of the reconstructed FS calculated within the TB model with  $V(q_{\text{CDW}})=0$  at  $k_x > 0$  and  $V(q_{\text{CDW}})=V(c^*-q_{\text{CDW}})$  at  $k_x < 0$ . The black contours are guide for the eyes of square and outer parts; dotted contours are for folded parts. (c) Zoom on the FS pockets measured in CeTe<sub>3</sub> with a photon energy of 55 eV.

the CDW is commensurate within discommensurate domains in order to create patterns of alternating short and long Te bonds. Such a picture would give more importance to the structural part of the CDW and implies deviations from the model of a nesting driven CDW. However, as shown in Ref. 19, the different couplings at  $(c^*-q_{\text{CDW}})$  and  $q_{\text{CDW}}$  more likely account for the anomalies observed in Ref. 17. We confirm this view and conclude that the CDW in RTe<sub>3</sub> is truly incommensurate and nesting driven although strongly 2D. We note that the CDW properties evolve in a nonmonotonous way for the heavy rare earths (Dy-Yb), which are notably characterized by the two successive CDW transitions.<sup>18</sup> This also gives rise to quite different FS reconstructions, which will be the subject of a different paper.<sup>44</sup>

This study gives a precise topology of the FS that could be compared to the frequencies of quantum oscillations observed in these systems.<sup>43</sup> Another important consequence is the estimation of the fraction of ungapped FS. This is independent of the distribution of weight along the pockets, as, by definition, it is the opposite on the pockets distant by  $q_{\text{CDW}}$  (see Fig. 17). Therefore, it is sufficient to integrate the FS contour up to  $k_x^0$  to obtain this fraction. We report on the right axis of Fig. 22 the percentage of the original FS contour that remains metallic. It increases from 35% in CeTe<sub>3</sub> to 55% in DyTe<sub>3</sub>. This is not such a small fraction, which appears consistent with the good metallicity of the samples.<sup>16,22</sup> The linear term in the heat capacity was also found to be reduced to 37% in LaTe<sub>3</sub> and 60% in YTe<sub>3</sub>, with respect to the calculated value, which is a similar order of magnitude.<sup>22</sup> On the other hand, a much smaller fraction (about 5%) was deduced from the analysis of optical measurements,<sup>23</sup> a discrepancy that needs to be understood.

### F. Stabilization of the charge density wave

So far, we have given a full description of the CDW in RTe<sub>3</sub> as a function of the interaction parameter  $V$ . To close the loop, it would be desirable to see which strength of the

electron-phonon coupling is required to stabilize such a CDW and whether the change in gap can be simply explained by the change in  $n(E_F)$  due to lattice expansion.

In the traditional nesting scenario, the CDW is stabilized when the gain of electronic energy overcomes the loss of elastic energy. The gain of electronic energy in the CDW state can be easily calculated with the interacting TB model of Sec. III A. It is due to the opening of the gap, which lowers the energy of these electrons on well nested parts of the FS. The examples of the DOS are given in Fig. 25(a), for one band,  $t_{\text{para}}=-1.8$  eV and  $t_{\text{perp}}=0.35$  eV, and different values of  $V$ . It has to be multiplied by 4 to obtain the DOS per cell (because of the two bands and two Te planes per cell). We take  $q_{\text{CDW}}$  from formula of Sec. III C for self-consistency. As expected, a gap of maximum value  $\Delta=2V$  opens.  $N(E_F)$  is reduced to 72% of the initial value at  $V=0.1$  eV and 55% at  $V=0.2$  eV. This is not directly comparable to our previous estimation of ungapped FS, as  $n(E_F)$  is not constant along the FS, but confirms that a significant residual metallic character is expected. With such a model, we can then calculate the electronic energy as a function of  $V$  for any  $t_{\text{para}}$  parameter, i.e., any value of  $n(E_F)$ .

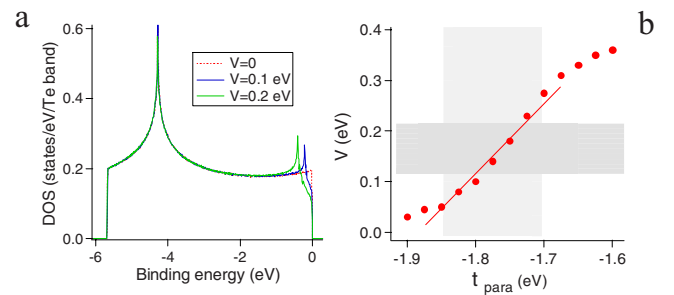


FIG. 25. (Color online) (a) Density of states in the TB model for indicated values of  $V$  ( $t_{\text{para}}=-1.8$  eV and  $t_{\text{perp}}=0.35$  eV). (b) Values of  $V$  stabilizing the CDW distortion as a function of  $t_{\text{para}}$ , assuming an elastic energy  $E=0.87*V^2$ . The shaded area indicates the regions sampled by RTe<sub>3</sub> compounds.

To calculate the stable value of  $V$ , we subtract the elastic energy. It is a quadratic function of  $V$ ,

$$E_{\text{dis}} = \frac{1}{2} M \omega_q^2 (\langle x_q \rangle^2 + \langle x_{-q} \rangle^2) = \frac{n(E_f)}{2\lambda} V^2,$$

where  $\lambda$  is defined to be a dimensionless electron-phonon coupling constant  $\lambda = g^2 n(E_f) / \hbar \omega_q$  ( $g$  is defined in Sec. III A and relates  $\langle x_q \rangle$  to  $V$ ). We find that  $E_{\text{dis}} = 0.87^* V^2$  allows us to find the gap values in the range of those observed experimentally. Results are shown by red filled circles as a function of  $t_{\text{para}}$  in Fig. 25(b). The zone expected for  $t_{\text{para}}$  is shaded, as well as the one corresponding to measured values of  $V$  deduced from Fig. 13. The theoretical variation is as large as the one observed experimentally, or even somewhat larger. This very large variation is due to the fact that, because of the imperfect nesting, increasing  $V$  does not only lower the energy of the electrons involved in the CDW but also increases their number. For  $V > 0.3$  eV, the entire FS would be gapped and the increase in the gap value indeed slows down.

As the energy differences involved in this process are very small, this rough model can only be taken as indicative. The qualitative trend is, however, robust and it is worth checking the order of magnitude of the parameters we use. The value of  $E_{\text{dis}}$  we use implies  $\lambda = 0.23$  (using the average TB value  $n(E_f) = 0.4$  states/eV/Te plane), a moderately strong electron-phonon coupling, very similar to that observed in quasi-1D CDW systems, such as  $\text{K}_{0.3}\text{MoO}_3$  ( $\lambda = 0.34$ ) or  $\text{NbSe}_3$  ( $\lambda = 0.53$ ).<sup>1</sup> The amplitude of the distortion in  $\text{CeTe}_3$  was estimated to be  $\langle x_q \rangle = 0.2 \text{ \AA}$ ,<sup>17</sup> which is rather large, as compared, for example, to  $0.05 \text{ \AA}$  in  $\text{K}_{0.3}\text{MoO}_3$  or  $0.09 \text{ \AA}$  in  $(\text{TaSe}_4)_2\text{I}$ .<sup>1</sup> As  $\langle x_q \rangle = 1 / \omega_q \sqrt{n(E_f) / 2\lambda M^* V}$ , and  $V = 0.2$  eV for  $\text{CeTe}_3$  (ARPES value), we get  $\omega_q \approx 5$  meV with the parameters used so far and  $M$  is the mass of one Te atom. Although the values of frequencies involved in the CDW are not precisely known, this seems a reasonable order of magnitude and supports this model as the origin of the CDW in  $\text{RTe}_3$ .

#### IV. CONCLUSIONS

We have presented a detailed investigation of the electronic structure of  $\text{RTe}_3$  based on a comparison between ARPES measurements and band calculations. The electronic structure is relatively simple, being built by broad  $p$ -type bands of Te atoms, where no strong correlation effects are expected. 3D couplings and the presence of rare earths in the slabs separating the Te planes are shown to have only minor incidences on the electronic structure of the planes. Therefore,  $\text{RTe}_3$  qualifies as a very interesting case study of a

simple 2D metal for ARPES. The major complication is the occurrence of a bilayer splitting, due to the two planes per unit cell, which we analyze and compare to band calculations. Despite these advantages, we find that a detailed analysis of the ARPES line shapes is difficult, probably because the surface curvature induces an extrinsic broadening of the spectra.

On the other hand,  $\text{RTe}_3$  definitely sets an ideal example of a nesting driven CDW system. We give a complete description of the ground state properties as a function of different  $R$  ions. We explain quantitatively the variation of the gap amplitude along the FS from its imperfect nesting, thanks to a simple TB model of the electronic structure. We show that the redistribution of the electronic density along the FS allows us to maximize the gap value at the Fermi level up to  $\Delta = 2V$ , where  $V$  is the electron-phonon interaction parameter. This implies a variation of the CDW wave vector  $q_{\text{CDW}}$  with  $\Delta$ , which we calculate and find in very good agreement with the experimental variation. We detail the topology of the FS, thanks to the observation of CDW shadow bands. We measure the extension of the residual metallic pockets as a function of the gap  $\Delta$ . The percentage of ungapped FS changes from 35% to 55%, depending on  $R$ .

Finally, we give a rough estimation of the balance between electronic and elastic energies needed to stabilize the CDW. We find that, for reasonable values of phonon frequencies ( $\omega_q = 5$  meV) and electron-phonon coupling ( $\lambda = 0.23$ ), we can reproduce the variation of the gap with the density of states quite well. This certifies that such models are relevant for the description of these materials. It seems that the large gap of  $\text{RTe}_3$  simply originates from the large displacements allowed in the square Te nets. The role of these displacements as a possible driving force for the transition would be interesting to define more precisely.<sup>26</sup> The recent observation of the transition to the normal state around room temperature for many  $\text{RTe}_3$  systems<sup>18</sup> and as a function of pressure in  $\text{CeTe}_3$  (Ref. 24) opens interesting possibilities to fully characterize this state. The transition temperatures deviate notably from the mean-field expectation, as often observed in CDW systems,<sup>1</sup> which emphasizes the importance of fluctuations.

#### ACKNOWLEDGMENTS

We thank E. A. Kim, A. Sacchetti, and L. Degiorgi for interesting discussions and A. V. Fedorov and A. F. Santander-Syro for help during measurements at ALS beamline 12. Work at Stanford is supported by DOE Office of Basic Energy Science, Division of Materials Science and Engineering, with Contract No. DE-FG03-01ER45929-A001.

<sup>1</sup>G. Grüner, *Density Waves in Solids* (Addison-Wesley, Reading, MA, 1994).

<sup>2</sup>E. Fawcett, *Rev. Mod. Phys.* **60**, 209 (1988).

<sup>3</sup>N. P. Ong and P. Monceau, *Phys. Rev. B* **16**, 3443 (1977), and references therein.

<sup>4</sup>H. Yao, J. A. Robertson, E. A. Kim, and S. A. Kivelson, *Phys.*

*Rev. B* **74**, 245126 (2006).

<sup>5</sup>M. Grioni, I. Vobornik, F. Zwick, and G. Margaritondo, *J. Electron Spectrosc. Relat. Phenom.* **100**, 313 (1999).

<sup>6</sup>B. Dardel, D. Malterre, M. Grioni, P. Weibel, Y. Baer, and F. Lévy, *Phys. Rev. Lett.* **67**, 3144 (1991).

<sup>7</sup>L. Perfetti, S. Mitrovic, G. Margaritondo, M. Grioni, L. Forro, L.

- Degiorgi, and H. Höchst, *Phys. Rev. B* **66**, 075107 (2002).
- <sup>8</sup>J. Schäfer, E. Rotenberg, S. D. Kevan, P. Blaha, R. Claessen, and R. E. Thorne, *Phys. Rev. Lett.* **87**, 196403 (2001).
- <sup>9</sup>P. Aebi, Th. Pillo, H. Berger, and F. Levy, *J. Electron Spectrosc. Relat. Phenom.* **117-118**, 433 (2001).
- <sup>10</sup>W. C. Tonjes, V. A. Greanya, R. Liu, C. G. Olson, and P. Molinié, *Phys. Rev. B* **63**, 235101 (2001).
- <sup>11</sup>M. D. Johannes, I. I. Mazin, and C. A. Howells, *Phys. Rev. B* **73**, 205102 (2006).
- <sup>12</sup>Y.-K. Kuo, F. H. Hsu, H. H. Li, H. L. Huang, C. W. Huang, C. S. Lue, and H. D. Yang, *Phys. Rev. B* **67**, 195101 (2003).
- <sup>13</sup>T. Nakagawa, H. Okuyama, M. Nishijima, T. Aruga, H. W. Yeom, E. Rotenberg, B. Krenzer and S. D. Kevan, *Phys. Rev. B* **67**, 241401(R) (2003).
- <sup>14</sup>E. DiMasi, M. C. Aronson, J. F. Mansfield, B. Foran, and S. Lee, *Phys. Rev. B* **52**, 14516 (1995).
- <sup>15</sup>E. DiMasi, B. Foran, M. C. Aronson, and S. Lee, *Phys. Rev. B* **54**, 13587 (1996).
- <sup>16</sup>E. DiMasi, B. Foran, M. C. Aronson, and S. Lee, *Chem. Mater.* **6**, 1867 (1994).
- <sup>17</sup>H. J. Kim, C. D. Malliakas, A. T. Tomic, S. H. Tessmer, M. G. Kanatzidis, and S. J. L. Billinge, *Phys. Rev. Lett.* **96**, 226401 (2006).
- <sup>18</sup>N. Ru, C. L. Condon, G. Y. Margulis, K. Y. Shin, J. Laverock, S. B. Dugdale, M. F. Toney, and I. R. Fisher, *Phys. Rev. B* **77**, 035114 (2008).
- <sup>19</sup>A. Fang, N. Ru, I. R. Fisher, and A. Kapitulnik, *Phys. Rev. Lett.* **99**, 046401 (2007).
- <sup>20</sup>G. H. Gweon, J. D. Denlinger, J. A. Clack, J. W. Allen, C. G. Olson, E. D. DiMasi, M. C. Aronson, B. Foran, and S. Lee, *Phys. Rev. Lett.* **81**, 886 (1998).
- <sup>21</sup>V. Brouet, W. L. Yang, X. J. Zhou, Z. Hussain, N. Ru, K. Y. Shin, I. R. Fisher, and Z. X. Shen, *Phys. Rev. Lett.* **93**, 126405 (2004).
- <sup>22</sup>N. Ru and I. R. Fisher, *Phys. Rev. B* **73**, 033101 (2006).
- <sup>23</sup>A. Sacchetti, L. Degiorgi, T. Giamarchi, N. Ru, and I. R. Fisher, *Phys. Rev. B* **74**, 125115 (2006).
- <sup>24</sup>A. Sacchetti, E. Arcangeletti, A. Perucchi, L. Baldassarre, P. Postorino, S. Lupi, N. Ru, I. R. Fisher, and L. Degiorgi, *Phys. Rev. Lett.* **98**, 026401 (2007).
- <sup>25</sup>M.-H. Whangbo and E. Canadell, *J. Am. Chem. Soc.* **114**, 9587 (1992).
- <sup>26</sup>M. D. Johannes and I. I. Mazin, arXiv:0708.1744 (unpublished).
- <sup>27</sup>B. K. Norling and H. Steinfink, *Inorg. Chem.* **5**, 1488 (1966).
- <sup>28</sup>J. Laverock, S. B. Dugdale, Zs. Major, M. A. Alam, N. Ru, I. R. Fisher, G. Santi, and E. Bruno, *Phys. Rev. B* **71**, 085114 (2005).
- <sup>29</sup>J. M. Luttinger, *Phys. Rev.* **119**, 1153 (1960).
- <sup>30</sup>K. Y. Shin, V. Brouet, N. Ru, Z. X. Shen, and I. R. Fisher, *Phys. Rev. B* **72**, 085132 (2005).
- <sup>31</sup>Y. Iyeiri, T. Okumura, C. Michioka, and K. Suzuki, *Phys. Rev. B* **67**, 144417 (2003).
- <sup>32</sup>For a review, see D. Malterre, M. Grioni, and Y. Baer, *Adv. Phys.* **45**, 299 (1996).
- <sup>33</sup>J.-S. Kang, C. G. Olson, Y. S. Kwon, J. H. Shim, and B. I. Min, *Phys. Rev. B* **74**, 085115 (2006).
- <sup>34</sup>We thank Daniel Malterre for pointing our attention to this.
- <sup>35</sup>Preliminary investigations into the effect of spin-orbit couplings suggest that the magnitude of what we refer to as bilayer splitting is somewhat influenced by these effects. However, the general behavior is not strongly modified and we did not include this complication into the presented calculation.
- <sup>36</sup>A. Damascelli, Z. Hussain, and Z.-X. Shen, *Rev. Mod. Phys.* **75**, 473 (2003).
- <sup>37</sup>D. R. Garcia, G.-H. Gweon, S. Y. Zhou, J. Graf, C. M. Jozwiak, M. H. Jung, Y. S. Kwon, and A. Lanzara, *Phys. Rev. Lett.* **98**, 166403 (2007).
- <sup>38</sup>A. Bansil, M. Lindroos, S. Sahrakorpi, and R. S. Markiewicz, *Phys. Rev. B* **71**, 012503 (2005).
- <sup>39</sup>S. Hüfner, *Photoelectron Spectroscopy* (Springer-Verlag, Berlin, 2003).
- <sup>40</sup>N. V. Smith, P. Thiry, and Y. Petroff, *Phys. Rev. B* **47**, 15476 (1993).
- <sup>41</sup>T. Valla, A. V. Fedorov, P. D. Johnson, and S. L. Hulbert, *Phys. Rev. Lett.* **83**, 2085 (1999).
- <sup>42</sup>R. Claessen, R. O. Anderson, J. W. Allen, C. G. Olson, C. Janowitz, W. P. Ellis, S. Harm, M. Kalning, R. Manzke, and M. Skibowski, *Phys. Rev. Lett.* **69**, 808 (1992).
- <sup>43</sup>N. Ru, R. A. Borzi, A. Rost, A. P. MacKenzie, J. Laverock, S. B. Dugdale, and I. R. Fisher, arXiv:0805.0661 (unpublished).
- <sup>44</sup>R. G. Moore, V. Brouet, R. He, J. Laverock, S. Dugdale, N. Ru, I. R. Fisher, and Z.-X. Shen (unpublished).